AD_____

Award Number: W81XWH-08-1-0701

TITLE: Micro and Nano-mediated 3D Cardiac Tissue Engineering

PRINCIPAL INVESTIGATOR: Rashid Bashir, Ph.D.

CONTRACTING ORGANIZATION: University of Illinois at Urbana-Champaign
Urbana, IL 61801

REPORT DATE: October 2011

TYPE OF REPORT: Annual

PREPARED FOR: U.S. Army Medical Research and Materiel Command
Fort Detrick, Maryland 21702-5012

REPORT DOCUMENTATION PAGE

Form Approved
OMB No. 0704-0188

1. REPORT DATE	2. REPORT TYPE	3. DATES COVERED
October 2011	Annual	24 September 2010 – 23 September 2011

4. TITLE AND SUBTITLE

Micro and Nano-mediated 3D Cardiac Tissue Engineering

5a. CONTRACT NUMBER

5b. GRANT NUMBER
W81XWH-08-1-0701

5c. PROGRAM ELEMENT NUMBER

6. AUTHOR(S)

Rashid Bashir, Ph.D.
Brian Cunningham, Ph.D., Hyunjoon Kong, Ph.D., Taher Saif, Ph.D., and
Larry Schook, Ph.D.
E-Mail: rbashir@illinois.edu

5d. PROJECT NUMBER

5e. TASK NUMBER

5f. WORK UNIT NUMBER

7. PERFORMING ORGANIZATION NAME(S) AND ADDRESS(ES)

University of Illinois at Urbana-Champaign
Urbana, IL 61801

8. PERFORMING ORGANIZATION REPORT NUMBER

9. SPONSORING / MONITORING AGENCY NAME(S) AND ADDRESS(ES)
U.S. Army Medical Research and Materiel Command
Fort Detrick, Maryland 21702-5012

10. SPONSOR/MONITOR'S ACRONYM(S)

11. SPONSOR/MONITOR'S REPORT NUMBER(S)

12. DISTRIBUTION / AVAILABILITY STATEMENT
Approved for Public Release; Distribution Unlimited

13. SUPPLEMENTARY NOTES

14. ABSTRACT

A grand challenge in cardiology since 1950s has been the development of an artificial heart that can replace a failing heart. This project envisages improving the care of battlefield-related cardiac injuries by providing novel methods to design and fabricate 3-D models of cardiac sub-components that would be critical in restoring the function of the heart.

Our current research investigated the significance of geometrical constraints on the process of mammalian myogenesis. Using 3D stereo-lithographic technology we developed a microvascular stamp that released multiple angiogenic growth factors and guided the formation of neovessels within patterns defined by the stamp. In order to test hydrogel constructs in vivo we developed a mouse myocardial infarction model. Using this model we have tested the creation, placement, and adhesion of patterned hydrogel heart patches. The fabrication process described in this work demonstrated for the first time, the ability to produce distributed feedback (DFB) biosensor surfaces uniformly over surface areas substantial enough to incorporate into standard format microplates. The fabrication was carried out in laboratory setting; however, all methods are compatible with extension of the process to a roll-based manufacturing paradigm.

15. SUBJECT TERMS
Biomaterials, Biosensors, Fabrication, Mechanobiology, Nanotechnology

16. SECURITY CLASSIFICATION OF:			17. LIMITATION OF ABSTRACT	18. NUMBER OF PAGES	19a. NAME OF RESPONSIBLE PERSON
a. REPORT	b. ABSTRACT	c. THIS PAGE			USAMRMC
U	U	U	UU	54	19b. TELEPHONE NUMBER *(include area code)*

ANNUAL REPORT

2010-11

Micro and Nano-mediated 3D Cardiac Tissue Engineering

Rashid Bashir, PI
University of Illinois
rbashir@illinois.edu

Submitted: November 23, 2011

Micro and Nanotechnology Laboratory
Center for Nanoscale Science and Technology*
Institute for Genomic Biology
www.illinois.edu

**The US Army TATRC-funded Micro and Nano-mediated 3D Cardiac Tissue Engineering is a project of the University of Illinois Center for Nanoscale Science and Technology (CNST) collaboratory*

Table of Contents

Contents

Annual Report (Rashid Bashir)

1. Award No. Army W81XWH-08-1-0701
2. Report Date: November 24, 2011
3. Reporting period: 2010-11
4. Principal Investigator: Rashid Bashir, University of Illinois
5. Telephone No.: 217-333-3097
6. Award Organization: University of Illinois
7. Project Title: **Micro and Nano-mediated 3D Cardiac Tissue Engineering**
8. Current staff, role and percent effort of each on project.

Staff Member	**Role**	**% Effort**
Rashid Bashir	PI	2%
Brian Cunningham	Co-PI	2%
Hyunjoon Kong	Co-PI	2%
Taher Saif	Co-PI	2%
Larry Schook	Co-PI	2%
Pinar Zorlutuna	Postdoc Assoc.	100%
Jae Hyun Jeong	Postdoc Assoc.	100%
Emerson De Souza	Postdoc Assoc.	100%
P. Bajaj	Graduate Res. Assistant	50%
V. Chan	Graduate Res. Assistant	50%
Kyle Textor	Graduate Res. Assistant	50%
Vikram Chaudhery	Graduate Res. Assistant	50%
Chun Ge	Graduate Res. Assistant	50%

Award Expenditures: September 24, 2008 to September 30, 2011

Award No. Army W81XWH-08-1-0701

COST ELEMENTS (CUMULATIVE)

Personnel	$581,361
Fringe Benefits	$113,806
Supplies	$133,345
Equipment	$787,138
Travel	$19,708
Other Direct Costs	$72,474
Subtotal	**$1,707,833**
Indirect Costs	$654,3733
Fee	$0
Total	**$2,362,206**

Research Groups

I. Rashid Bashir, PI
II. Taher Saif, co-PI
III. Larry Schook, co-PI
IV. Hyun Joon Kong, co-PI
V. Brian Cunningham, co-PI

SECTION I: Annual Report Overall Project

This section describes briefly the salient aspects of the research for the 2010-11 reporting period. Additional details about sub-tasks are provided in subsequent sections.

I. SUMMARY OF WORK

The overall objective of our project is to help improve the care of battlefield-related cardiac injuries by providing novel methods to design and fabricate 3-D models of cardiac sub-components critical in restoring heart function.

Our current research investigated the significance of geometrical constraints on the process of mammalian myogenesis. In addition development of microvasculature *in-vivo* and *in-vitro* using a cell-laden polymeric stamp was undertaken.

Skeletal myogenesis is a highly orchestrated terminal differentiation process. In this study, we investigated the influence of two-dimensional geometrical cues on the differentiation of C2C12 myotubes by using three different geometries. The results have potential implications in engineering skeletal muscle tissues and designing muscle cell bio-actuators.

Using 3D stereo-lithographic technology we developed a microvascular stamp that released multiple angiogenic growth factors and guided the formation of neovessels within patterns defined by the stamp.

The research included the study of the: a) effect of myocyte network on local and global contraction performance, b) behavior of myocyte on thin pdms-membranes and c) effect of myocyte alignment on topographically patterned substrates.

In order to test hydrogel constructs *in vivo* we developed a mouse myocardial infarction model. Using this model we have tested the creation, placement, and adhesion of patterned hydrogel heart patches.

The fabrication process described in this work demonstrated for the first time, the ability to produce distributed feedback (DFB) biosensor surfaces uniformly over surface areas substantial enough to incorporate into standard format microplates. The fabrication was carried out in laboratory setting; however, all methods are compatible with extension of the process to a roll-based manufacturing paradigm.

II. INTRODUCTION

The regeneration of cells and tissue after injury or trauma is critical to medical and civilian communities. Cardiac injuries and regenerative engineering poses specific challenges since cardiac myocytes, the primary cells responsible for the mechanical beating of the heart muscle, do not regenerate. The cardiac system poses a significantly challenging problem in tissue engineering due to the complex 3-dimensional mechano-actuation properties of the cardiac cells.

A grand challenge in cardiology since early 50s is the development of an artificial heart that can replace a failing heart. Until today, artificial heart is used only for the temporary use (hrs) until a healthy donor heart is found. The latter is difficult to get, and is often rejected by the body after successful replacement. This very limited success in heart replacement, in spite of considerable effort and resources invested so far, calls for a new paradigm in the approach of heart replacement. This project attempts to offer such a paradigm by proposing to "grow" the heart or its components from the basic building blocks, namely the cells (differentiated cardiomyocytes) of the patient, biomaterials design, namely the hydrogel scaffolds to house the cells, and nanotechnology, namely the stereo-lithographically-patterned 3D substrate. New knowledge on cells' response to mechanical cues, and recent findings on cardiomyocyte functionality on mechanically tuned substrates from our labs form the basis for the project. In summary, stem cell differentiation in scaffolds, novel 3-D fabrication technologies, use of the appropriate biomaterials, integration of peptides for cardiac cell attachment and cell growth, the characterization of the scaffold materials and the transmembrane proteins, and cardiac cell mechanics are all critical elements of a comprehensive design approach proposed in this project for 3-D cardiac tissue engineering.

This project offers the use of 3-D stereolithography for fabricating the hydrogel scaffolds with cardiac cells, and nanoscale mechanical and optical tools for characterization of cardiac cells and their interactions with the scaffolds. ***Our objectives are to integrate these multi-disciplinary efforts and develop the strategies and methodologies for novel designs of 3-D components of an artificial heart.***

The project overview and research thrusts for each of the co-PIs are provided in the figure below, and the following table enlists third year project goals:

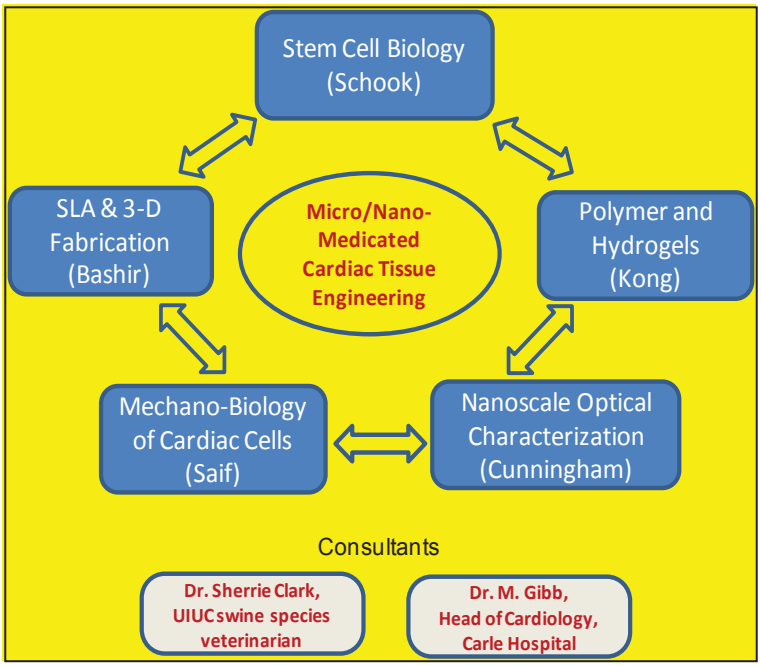

	Year 3 Project Goals
1	Interface DFB laser biosensor and detection instruments w/ engineered cell scaffolds and observe cell membrane activity during cell seeding, proliferation, exposure to pulsating flow, exposure to chemical compounds/ growth media.
2	To demonstrate and characterize the capability of using SL to design and generate complex 3-D tissue with tunable architecture
3	Measure cardiac myocyte beating frequency versus material stiffness.
4	Develop 2D cantilever substrates with cardiac cells to explore the range of deformation and the frequencies of the cantilevers.
5	Demonstrate improved cardiac tissue function in hydrogels with properties optimized via *in vitro* cell studies.

III. BODY

Potential Military Relevance. Battlefield trauma resulting in a variety of injuries is of significant concern to our military and civilian administration. Tissue engineering or regenerative medicine offers viable alternatives to counter many such injuries. ***Our project envisages improving the care of battlefield-related cardiac injuries by providing novel methods to design and fabricate 3-D models of cardiac sub-components that would be critical in restoring the function of the heart***. According to the report on 'Capturing the power of biomaterials for military medicine'(NRC Report,2004), four areas in which enhancement of biomaterials and biotechnology will have a major impact on acute, chronic, and rehabilitation care in military medicine are (1) wound care, (2) tissue engineering, (3) drug delivery, and (4) physiological sensors and diagnostics. Our target area of research in cardiac tissue engineering, addresses one of the critical needs for the care in military medicine. The ultimate goals of our research are to resolve chronic medical problems and ultimate rehabilitation of injured military personnel (NRC Report, 2004). Our approach of using a mobilized cell population also provides flexibility in obtaining human MSCs in the field. They could be harvested from the soldiers and banked so they would have a source of their own cells. This approach is much faster and safer than bone marrow derived cells. The scaffolds we will develop could also be loaded with drugs that would be released over time to allow minimizing rejection by the body. Clearly, new methods for development of engineered tissues will have many applications beyond cardiac tissue engineering to engineering of vessels, skin, and many other organs.

IV. KEY RESEARCH ACCOMPLISHMENTS

- Using stereolithography a microvascular stamp was developed that released multiple angiogenic growth factors and guided the formation of neovessels within patterns defined by the stamp.

- Observed that myocyte-network also was dependent on the region the cells were extracted from the heart.

▪Four key capabilities of the stereolithography assembly (SLA) were established, these included to: (i) pattern tissue-like hydrogels into complex 3D constructs, (ii) encapsulate cells into these hydrogel constructs, (iii) incorporate multiple materials, cell types, and proteins into distinct layers on the same construct, and (4) maintain cell viability, spreading, and proliferation over long periods in culture.

▪A method was developed to provide excellent spatial control over the matrix architecture into the gel using a stereolithographic assembly (SLA). A 'living' microvascular stamp was created that released multiple angiogenic factors and subsequently created neovessels with the same pattern as those engraved on the stamp.

▪Improved mouse myocardial infarction model.

▪Production of distributed feedback (DFB) biosensor surface was demonstrated uniformly over surface areas substantial enough to incorporate into standard format microplates.

V. REPORTABLE OUTCOMES

List of Publication Accepted by Peer-Reviewed Journals

- C. Cha, S.Y. Kim, L. Cao, H. Kong, Decoupled control of stiffness and permeability with a cell-encapsulating poly(ethylene glycol) dimethacrylate hydrogel. ***Biomaterials*** (2010) 31, 4864-4871

- R.J. DeVolder, H. Kong, Three dimensionally flocculated proangiogenic microgels for neovascularization. ***Biomaterials*** (2010) 31, 6494-6501

- Y. Liang, T.W. Jensen, E.J. Roy, C. Cha, R.J. DeVolder, R.E. Kohman, B.Z. Zhang, K.B. Textor, L.A. Rund, L.B. Schook, Y.W. Tong, H. Kong, Tuning the non-equilibrium state of a drug-encapsulated poly(ethylene glycol) hydrogel for stem and progenitor cell mobilization. ***Biomaterials*** (2011) 32, 2004-2012

- J.H. Jeong, V. Chan, C. Cha, P. Zorlutuna, C. Dyck, K.J. Hsia, R. Bashir, and H. Kong., 'Living' microvascular stamp for patterning of functional neovessels; Orchestrated control of matrix property and geometry. ***Advanced Materials*** (2011) in press.

- Bajaj P., Reddy Jr. B., Millet L., Wei C., Zorlutuna P., Bao G. and Bashir R., "Patterning the differentiation of C2C12 skeletal myoblasts", *Integrative Biology* 2011; 3: 897-909 (*Inside Cover Article*).

Abstract and Conference Presentations

- J.H. Jeong, V. Chan, C. Cha, P. Zorlutuna, Rashid Bashir, and Hyunjoon Kong, "In situ cell encapsulation into a vascularized hydrogel matrix using a SLA." Outstanding research award in stem cell and regenerative medicine, Tissue Regenerative Symposium, March 24, 2010, Chicago, IL, USA.

- J.H. Jeong, V. Chan, C. Cha, P. Zorlutuna, R. Bashir, H. Kong, "Assembly of functional neovessels using a stereolithogrphically assembled hydrogel." 1st place poster winner on Regenerative Biology and Tissue Engineering, October 22, 2010, Institute for Genomic Biology, Champaign, IL, USA.

- J.H. Jeong, V. Chan, C. Cha, P. Zorlutuna, R. Bashir, H. Kong, "Assembly of functional neovessels using a stereolithographic hydrogel matrix." Oral presentation, American Chemical Society (ACS) National Spring Meeting, March, 2011, Anaheim, USA.

- J.H. Jeong, V. Chan, C. Cha, P. Zorlutuna, R. Bashir, H. Kong, "Assembly of functional neovessels using a stereolithographic hydrogel matrix." 2011 Society For Biomaterials (SFB) Annual meeting, April 13-16, Orlando, FL, USA.

- J.H. Jeong, V. Chan, C. Cha, P. Zorlutuna, C. Sukotjo, R. Bashir, H. Kong, "Independent control stiffness and permeability of a cell-encapsulating hydrogel for tissue engineering." Oral presentation, 2011 BMES Annual meeting, October 12-15, 2011, Hartford, USA.

- J.H. Jeong, V. Chan, C. Cha, P. Zorlutuna, R. Bashir, H. Kong, "Independent control stiffness and permeability of a cell-encapsulating hydrogel; Integration of Bio-inspired material chemistry and microfabrication." Oral presentation, 2011 AIChE Annual Meeting, October 16-21, 2011, Minneapolis, MN, USA.

- Molly Melhem, Tor Jensen, Jae Hyun Jeong, Vincent Chan, Rashid Bashir, Hyunjoon Kong, Lawrence Schook. A Cardiac Patch for Delivering Therapeutic Stem Cells to the Heart Following Myocardial Infarction. University of Illinois, Chicago. Third Stem Cell and Regenerative Medicine Symposium. May 20, 2011

List of Manuscripts in Preparation

- "Plastic-based distributed feedback laser biosensors in microplate format," Y. Tan, A. Chou, C. Ge, M. Lu, W. Goldshlag, J. Huang, A. Pokhriyal, S. George, and B.T. Cunningham, IEEE Sensors Journal, Accepted, July 2011.

- C. Ge, J. Zheng, C.Wagner, M. Lu, B. T. Cunningham and J. G. Eden, "Optically tunable ring external-cavity laser", IEEE photonics conference, Arlington VA, October 2010.

- Tan, Y.; Ge, C.; Chu, A.; Lu, M.; Goldshlag, W.; Huang, C.; Pokhriyal, A.; George, S.; Cunningham, B.; "Plastic-Based Distributed Feedback Laser Biosensors in Microplate Format," Sensors Journal, IEEE, vol.PP, no.99, pp.1, 0 doi: 10.1109/JSEN.2011.2163933

VI. CONCLUSION

The dynamic of myocyte network and its effect on its own evolution has been observed, revealing that the global myocyte dynamic is severely affected by local effects such as resistance to motion provoked by sticky debris and tissue fragments on the substrates. Alignment of myocytes on patterned substrates is not obvious and cannot be anticipated, as it is not only substrate-dependent but also on the type of myocyte. A rigorous investigation is needed to clarify this question. For instance, the current results show the tendency of ventricle myocytes to align and to build long connections up to 2 mm but this did not occur for atrial myocytes. The experiment and results of long living myocytes on PDMS membrane motivates new investigations on the effect of mechanical environment on myocytes using this device. Understanding why myocytes die *in vitro* studies can be fundamental for improve *in vivo* cell regeneration.

With the current *in vivo* model we will perfect the production and application of hydrogel-based heart patches generated by stereolithography assembly (SLA). Both encapsulated cells and drugs will be tested for their ability to reduce cardiac damage following myocardial infarction. Initial experiments in the mouse model will allow for the scaling of similar patches in larger, more relevant animal models in the future. Current adhesive patch designs will also have direct relevance to other applications in soft tissues requiring prolonged exposure of target tissues to cells and/or drugs stabilized by hydrogel matrices.

We have developed a ‘living’ microvascular stamp that releases multiple angiogenic factors and subsequently creates neovessels with the same pattern as that engraved in the stamp. The stamp consists of live cells that secrete angiogenic factors, an engineered hydrogel matrix that promotes cellular expression of angiogenic factors, and a three-dimensional (3D) geometry that localizes the angiogenic factors within the pattern. When the stamp was implanted on a target site, it created the desired pattern of neovessels based on 3D geometry of the stamp, allowing the control of the density and spacing of blood vessels.

Overall, this study demonstrated that the bulk properties of the cardiac patch played a critical role in activating cellular expression of proangiogenic factors and the geometry of the microchannel patterns regulated the local distribution of proangiogenic factors on the implant site. These two material variables were orchestrated to spatially organize neovessels into the predefined pattern of the cardiac patch. This patch can be readily modified for clinical settings

with other cell types, such as mesenchymal stem cells, which also endogenously express multiple proangiogenic growth factors. In the near future, we plan to incorporate this cardiac patch into an *in vivo* myocardial infarct animal model to see if it can stimulate the growth of spatially organized neovessels at the site of injury, thereby preventing scarring and deterioration of the heart.

The fabrication process described in this work demonstrated for the first time, the ability to produce DFB biosensor surfaces uniformly over surface areas substantial enough to incorporate into standard format microplates. Although the fabrication was carried out in a laboratory setting, all methods are compatible with extension of the process to a roll-based manufacturing paradigm. In particular, the nanoreplica molding approach used in this work has been implemented upon continuous rolls of plastic film in a step-repeat process that can utilize a master wafer for thousands of iterations without damage. ***Incorporation of a label-free sensor into a microplate format represents an important step in the development of a technology that can be accepted into pharmaceutical high throughput screening***, as this liquid handling method is heavily utilized for assay automation and integration with standard liquid handling systems. A substantial advantage of the DFBLB sensor surface is that any region on the surface is a sensor, and as a result, capture molecules and illumination can occur at any location. ***We also envision a label-free surface scanning detection approach***, in which the excitation spot is rastered across the DFBLB surface to generate a spatial map of biomolecular or cellular binding for applications such as label-free microarrays and label-free cell attachment imaging.

SECTION II: Annual Report from Project Subgroups

Research Group: Rashid Bashir

Period Aug'10 to Aug'11

Patterning the differentiation of C2C12 myoblast

Research Description and Potential Impact:

Skeletal myogenesis is a highly orchestrated terminal differentiation process in which the proliferating mono-nucleated myoblasts differentiate and fuse to form multi-nucleated myotubes. In this study, we investigated the influence of two-dimensional geometrical cues on the differentiation of C2C12 myotubes by using three different geometries - lines of different widths, tori of different inner diameter, and hybrid structures (linear and circular features with different arc degrees). These different geometries were created by micro-contact printing (μCP) of fibronectin on the surface of Petri dishes. The differentiation of C2C12 cells was quantified; we report the differentiation parameters of (1) fusion index, (2) degree of maturation, (3) alignment, and (4) response to electrical pulse stimulation (EPS). These results can have implications in engineering skeletal muscle tissues and designing muscle cell bio-actuators.

Research Objectives:

The overall objective of the current research was to investigate the significance of geometrical constraints on the process of mammalian myogenesis.

Aim 1: To create the different geometrical patterns on two-dimensional Petri dishes.

Aim 2: Quantify the difference in the degree of differentiation on the different patterns by using the differentiation parameters of (1) fusion index, (2) degree of maturation, (3) alignment, and (4) response to electrical pulse stimulation (EPS).

Aim 3: Investigate the reasons for the difference in the myogenesis on the difference geometries.

Progress towards the Objectives:

Aim 1: Creating different geometrical patterns on the Petri dishes.

Fig. 1 shows the fluorescent images C2C12 cells patterned on the

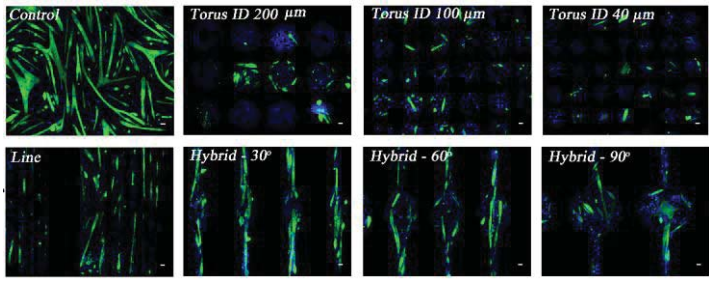

Fig. 1: Fluorescent images of the cells on the different μCP cell islands – lines of different width (300 μm, 150 μm, 80 μm, 40 μm, 20 μm, and 10 μm), tori of different inner diameter (40 μm, 100 μm, and 200 μm), and hybrid patterns of different arc degree (30^o, 60^o and 90^o) on day 7. Cells were stained for anti-MHC (green) and nucleus (blue) (Scale bar = 100 μm).

different geometries at the end of seven days. Approximately, 75,000 cells were seeded on each substrate and observed for nine days resulting into an initial cell seeding of 7800 cells/cm^2 for the 35 mm Petri dish. We patterned three different geometries, with multiple sized structures for each geometry. For linear patterns, we used 2000 μm long lines of various widths (300 μm, 150 μm, 80 μm, 40 μm, 20 μm, and 10 μm). Torus patterns consisted of the various inner diameters (ID) (40 μm, 100 μm, and 200 μm) and outer diameters (OD) (200 μm, 260 μm and 360 μm). Hybrid patterns were fabricated to produce a linear element with a central circular belly; the linear element was 100 μm wide, whereas the arc of the circular belly was either 30^o, 60^o or 90^o. The fourth, unpatterned substrate (control) was the unpatterned Petri dish.

Aim 2: Quantify the difference in the degree of differentiation on the different patterns.

C2C12 myoblasts when deprived of serum undergo cell cycle arrest and start to fuse together to form multinucleated myotubes. Myotubes serve as the building blocks for skeletal muscle, thus understanding the differentiation process of C2C12 skeletal myoblasts *in vitro* has the potential to resolve mechanisms of the myogenic differentiation process *in vivo* as well. Fusion index was calculated as the ratio of nuclei number in myocytes with two or more nuclei versus the total number of nuclei. Hybrid structures with the smallest arc degree (hybrid 30^o) showed the best results for all four differentiation parameters. The hybrid 30^o pattern exhibits a ~2-fold increase in the fusion index when compared to the line patterns and ~3-fold increase when compared to the toroid pattern. Hybrid 30^o (45.38 ± 2.57 %) showed greater than 1.5 fold differentiation compared to hybrid 60^o (29.20 ± 1.20 %) and hybrid 90^o (25.71 ± 2.62 %). In contrast, there was no significant difference in the differentiation of C2C12 myotubes on the linear patterns of different widths. However, myotubes on the linear patterns showed a significant decrease in differentiation when compared to the control at $p < 0.01$. The large width line pattern (300 μm) was used to mimic the unpatterned control. Presumably, even thicker patterns are required so that the cells on these patterns start mimicking the properties of the cells on the unpatterned control. Similar results were observed for the circular geometry. There was no significant difference of differentiation between the toroids of different IDs; when compared to controls, all of the toroids showed a decrease in differentiation at $p < 0.01$. Fig 2A summarizes the fusion index for all the different geometries by incorporating the highest for each type.

The maturation index (% myotubes $\geq$ 5 nuclei) was also used as a parameter to evaluate the differentiation of C2C12 myotubes. The maturation index can also be used to quantify the size of the myotube; a higher maturation index represents a myotube which is larger in size. The hybrid 30^o pattern, which showed highest fusion index, also shows the highest maturation index for the myotubes. The maturation index for the hybrid 30^o (73.09 ± 4.41 %) pattern was statistically higher ($p < 0.05$) than that for the control (60.24 ± 2.19 %), hybrid 60^o (55.11 ± 3.83 %) and hybrid 90^o (46.71 ± 3.91 %) ($p < 0.01$). There was no statistically significant difference in the size of the myotubes on line patterns of different widths. Also, the toroid patterns showed similar results where no significant difference could be seen in the maturation index for tori of different inner diameter. However, each of them showed smaller maturation for the myotubes when compared to the control. Fig 2B summarizes the maturation index for all the different geometries by incorporating the highest for each type.

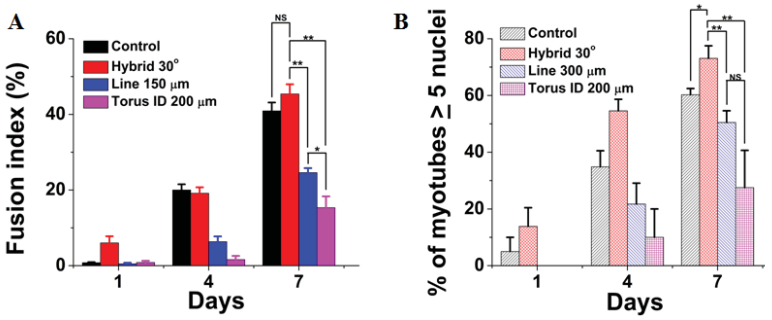

Fig. 2: Quantification of the differentiation parameters of fusion and maturation index on the different geometries. (A) The highest from each of the different cell islands are plotted together to show the geometry that maximized the fusion index of C2C12 cells - hybrid 30°. (B) The highest maturation index for the different geometries. Significance ** $p < 0.01$, *$p < 0.05$, and *NS = not significant*. Data is represented as mean ± S.E.M (n = 10 patterns).

Controlling the alignment of cells is critical for any tissue engineered graft. *In vivo*, many cells/tissues like neural cells, cardiac muscle, skeletal muscle, corneal tissue, vascular tissue have a very high degree of alignment associated with them which in turn enhances their functionality. In particular, for skeletal and cardiac muscle, alignment of cells is extremely important in order to maximize the contractile power of the tissue. We therefore investigated the alignment of myotubes on the micropatterned cell islands using two-dimensional FFT. Myotubes on the control (unpatterned) substrate showed no distinguishable peak in the two-dimensional FFT alignment plot indicating that there is no alignment of myotubes on this substrate. This was further confirmed by looking at the angle of deviation of myotubes from the principal axis and only less than 20% myotubes showed 15° or less deviation. As expected, myotubes on the linear patterns showed a very high degree of cell alignment. Myotubes on the line (width 80 μm) showed a very sharp narrow peak which is indicative of high degree of cell alignment. More than 90% of the myotubes showed less than 15° of deviation from the principal (long) axis of the linear geometry. However, as the width of the linear geometry was increased from 80 μm to 300 μm, a sharp decrease in the alignment of myotubes was seen. Less than 40% of the myotubes now showed 15° or less of cellular deviation. Also, the two-dimensional FFT alignment plot is now much broader which indicates more than one axis of alignment. By quantifying the alignment of myotubes on the hybrid patterns, we see that hybrid 30° patterns (width of the linear portion is about 100 μm) showed the highest fusion and maturation index for the myotubes also showed a very high degree of myotube alignment. Almost 90% of the myotubes showed 15° or less of deviation while 100% of the myotubes were within 30° of deviation from the principal axis of the geometry. The two-dimensional FFT alignment plot also showed a narrow high peak indicating high degree of alignment for the myotubes. However, the alignment of myotubes for the hybrid 90° patterns (width of the linear portion is about 100 μm) was not very high. Less than 30% of the myotubes showed $\leq$ 15° of deviation from the principal axis of the geometry and the two-dimensional FFT alignment plot did not show peaks. Taken together, these results suggest that as the width of the linear portion in the geometry is increased, the degree of alignment goes down. Also, by adding a curvature to the linear geometry, the degree of alignment decreases. However, for small curvatures, the deviation is small as seen for the hybrid 30° pattern. As the arc degree of the curvature increases the alignment decreases substantially as seen for the hybrid 90° pattern.

Muscles being an electrogenic tissue, their development are closely linked to their electrical activity. Therefore, we were interested in looking at the contraction of these cells using an electrical pulse stimulator. First, we investigated the affect of frequency on the contraction of myotubes. The myotubes contracted at the rate at which a frequency pulse from the waveform generator was applied to them. The data suggests that it is possible to synchronize the frequency of contractions of myotubes to the electrical pulse frequency. The displacement of myotubes under the application of an electric filed for cells on different patterns was quantified. Twitch responses of myotubes were observed at lower frequencies (1 – 10 Hz) while tetanic contractions were observed at higher frequencies (≥ 30 Hz). The displacement amplitude slightly increased from day 4 to day 7 for all the different patterns as can be seen in Fig. 3. The highest displacement was seen for the hybrid 30° pattern with the average being 1.24 ± 0.16 µm. The line pattern (width 300 µm) showed the second highest displacement which was 0.71 ± 0.09 µm followed by the torus (ID 200 µm) pattern which registered an average of 0.60 ± 0.09 µm displacement. Patterns with higher fusion/maturation index show higher displacements.

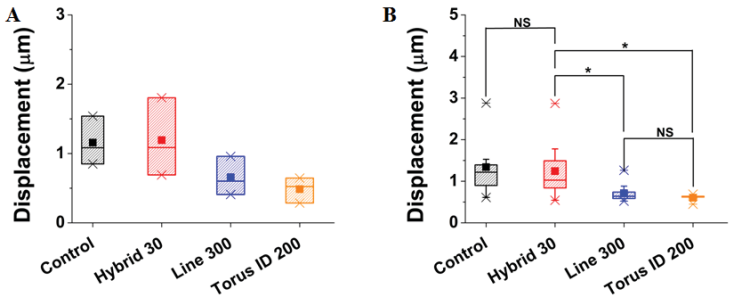

Fig. 3: Box plots showing the average displacements of the patterns on (A) day 4 (n = 3) (B) day 7 (n = 5 for the torus, n = 7 for line (300 µm) and n = 13 for control and hybrid 30° patterns). The mean is represented as the solid square in the box plot and the top and bottom (x) show the 99 percentile and 1 percentile respectively. Significance, *$p < 0.05$, and *NS = not significant*. Data is represented as mean ± S.E.M.

Aim 3: Investigate the reasons for the difference in the myogenesis on the difference geometries.

The same numbers of cells were seeded on each of the substrates (initial seeding density was the same on all patterns), but the outcome shows different cell densities for each pattern. This could be attributed to the different areas and different number of patterns on each chip. Since, it is known that myogenesis is density dependent process; we wanted to confirm that the differences in the differentiation parameters of fusion and maturation index cannot be attributed to the different densities of cells on the different patterns. Fig. 4A shows the average cell density on the different patterns plotted together with the fusion index for day 7. Hybrid 30° pattern showed the highest average cell density and the highest fusion index. The inset for Fig. 4A shows cell density plotted against the fusion index of cells. The Pearson's correlation coefficient is 0.495 which suggests that there is a very low level of associativity between fusion index and cell density. Even though the highest cell density showed the highest cell fusion, density cannot be the dominant factor because of these differences in the fusion indices are seen on the different patterns. For example, there is a statistically significant difference between the fusion index of the hybrid 30° and the hybrid 60° pattern at $p < 0.01$. However, for the two same geometries, there is no significant difference in the density. In contrast, the linear geometries (20 µm versus 150 µm) show no significant difference in the fusion indices while there is a statistically

significant difference in the densities between these two different structures. The same argument also holds true for Fig. 4B where the cellular density and maturation index is plotted against the type of pattern while the inset shows them plotted against each other. The Pearson's correlation coefficient is 0.551 which means that there is low associativity between the two parameters – maturation index and cellular density. Under our given experimental conditions we can conclude that the effects of maturation index and fusion index on the different patterns are not likely to be attributed to the differences in densities on those patterns. Rather, the data suggests that other inherent mechanisms and cellular pathways exert a dominant influence on this fusion and maturation process for different micropatterned geometries.

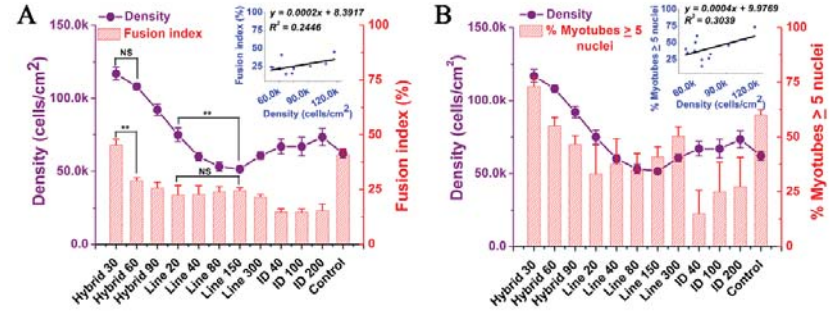

Fig. 4: (A) The fusion index and density of C2C12 myotubes on the various micropatterned cell islands on day 7. The inset shows a scatter plot of the fusion index and the density of C2C12 myotubes. (B) The maturation index (% myotubes ≥ 5 nuclei) and density of C2C12 myotubes on the various micropatterned cell islands on day 7. The inset shows a scatter plot of the maturation index and the density of C2C12 myotubes. Significance ** $p < 0.01$, *$p < 0.05$, and *NS = not significant*. Data is represented as mean ± S.E.M (n = 10 patterns).

Protein micro patterning can be used to mimic, at a fundamental level, the in vivo architecture of the tissues and to study cellular differentiation in vitro. We conclude that geometrical cues influence differentiation process of C2C12 myoblasts. We investigated the differentiation of C2C12 myoblasts on three main geometries – linear, circular and a hybrid pattern which combined linear and circular features together in one geometrical unit. Hybrid 30o pattern emerged as the most optimum geometry to maximize the differentiation of C2C12 myotubes.

Bajaj P., Reddy Jr. B., Millet L., Wei C., Zorlutuna P., Bao G. and Bashir R., "Patterning the differentiation of C2C12 skeletal myoblasts", *Integrative Biology* 2011; 3: 897-909 (*Inside Cover Article*).

Development of microvasculature In-vivo and In-vitro using a cell-laden polymeric stamp

Research Description and Potential Impact:

Using stereolithography, we developed a microvascular stamp that releases multiple angiogenic growth factors and guides the formation of neovessels within patterns defined by the stamp. The stamp consists of living cells that secrete angiogenic growth factors, an engineered hydrogel matrix that promotes cellular expression of angiogenic growth factors, and a three-dimensional (3D) geometry that localizes the angiogenic growth factors within the patterns. The potential

impact is the development of functioning vasculature that supports biological components *in vitro* (*i.e.* cell clusters in a bio-bot) or regeneration of chronic diseases or ischemic wounds *in vivo*.

Research Objectives:

The overall goal is to build a microvascular patch using 3D stereo-lithographic technology to guide and pattern blood vessel formation.

Aim 1: To adapt the 3D stereo-lithographic apparatus for biological components (*i.e.* living cells, photopolymerizable hydrogels, and signaling proteins)

Aim 2: To develop a novel photopolymerizable hydrogel matrix that decouples elastic modulus and swelling ratio

Aim 3: To demonstrate blood vessel patterning using microvascular stamps implanted on chick chorioallantoic membranes (CAMs)

Progress toward Objectives and Significant Achievements:

Aim 1: To adapt the 3D stereo-lithographic apparatus for biological components

Figure 1

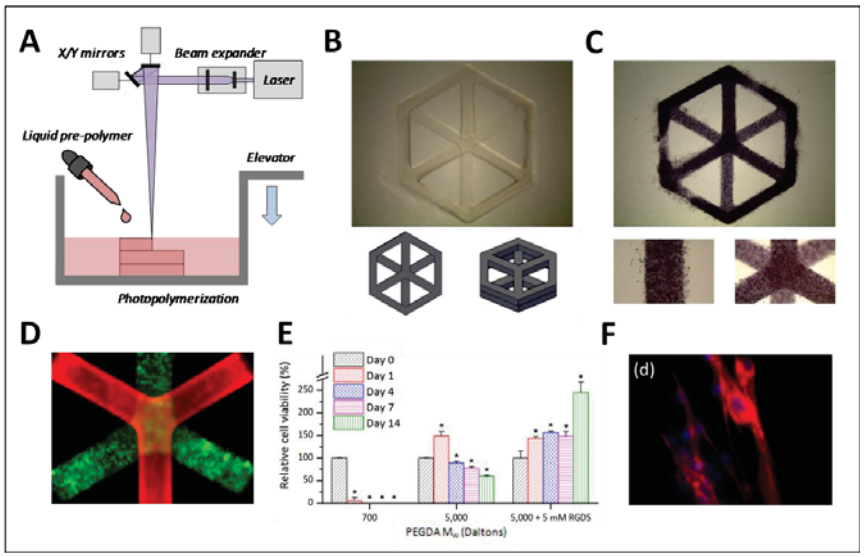

First, we introduced the capabilities of the SLA technology. The SLA is a computer-aided design (CAD) based rapid prototyping system that provides excellent spatial control over the matrix architecture (Fig. 1A). The core concept is to use a UV laser to polymerize a liquid photopolymer by repetitive deposition and processing of individual layers into a desired 3D pattern. The SLA is both reproducible and high-throughput. In our recent work, we established four key capabilities of the SLA. It can be used (1) to pattern tissue-like hydrogels into complex 3D constructs (Fig. 1B), (2) to encapsulate cells into these hydrogel constructs (Fig. 1C), (3) to incorporate multiple materials, cell types, and proteins into distinct layers on the same construct (Fig. 1D), and (4) to maintain cell viability, spreading, and proliferation over long periods in culture (Fig. 1E, 1F).

Aim 2: To develop a novel photopolymerizable hydrogel matrix that decouples elastic modulus and swelling ratio

The dream to manufacture clinically-viable tissues and organs jump-started the field of tissue engineering and regenerative medicine in the 1990s to accommodate for the shortage of organ donors. Today, the shortage still exists and the development of tissue equivalents has stalled. This is partly due to the lack of advanced vascularization strategies for controlling the direction and spacing of neovessel growth. Metabolically-demanding tissues such as those in the heart, brain, and liver need capillaries within 500 μm of each other in order to have sufficient oxygen tension. Therefore, vascularization is a central component in the design of any approach to tissue engineering. The aim of our work is to focus on enabling technologies to develop a clinically-viable vascularization method through the combined use of a 3D stereo-lithographic (SLA) patterning technique and a novel growth factor-cell-matrix combination therapy.

We developed a novel poly(ethylene glycol) diacrylate (PEGDA) and methacrylic alginate (MA) hydrogel matrix (Fig. 2A) capable of stimulating encapsulated cells to release multiple proangiogenic growth factors, while maintaining structural integrity at the implant site. The elastic modulus and swelling ratio were tuned to prepare a rigid, yet permeable PEGDA-MA hydrogel so that the cell-encapsulated hydrogel would not only remain stable, but also support cellular expression of proangiogenic factors (Fig. 2B). The role of MA was to reverse the typical inverse relationship between stiffness and bulk permeability that conventional hydrogel systems have. The increase in the bulk permeability of the PEGDA-MA hydrogel translated into improved cell viability compared to PEGDA only (Fig. 2C). Subsequently, fibroblasts that are known to endogenously express proangiogenic factors were encapsulated into the PEGDA-MA hydrogels. As revealed by microarray analysis, fibroblasts encapsulated within PEGDA-MA hydrogels expressed large amounts of multiple proangiogenic factors (Fig. 2D).

Figure 2

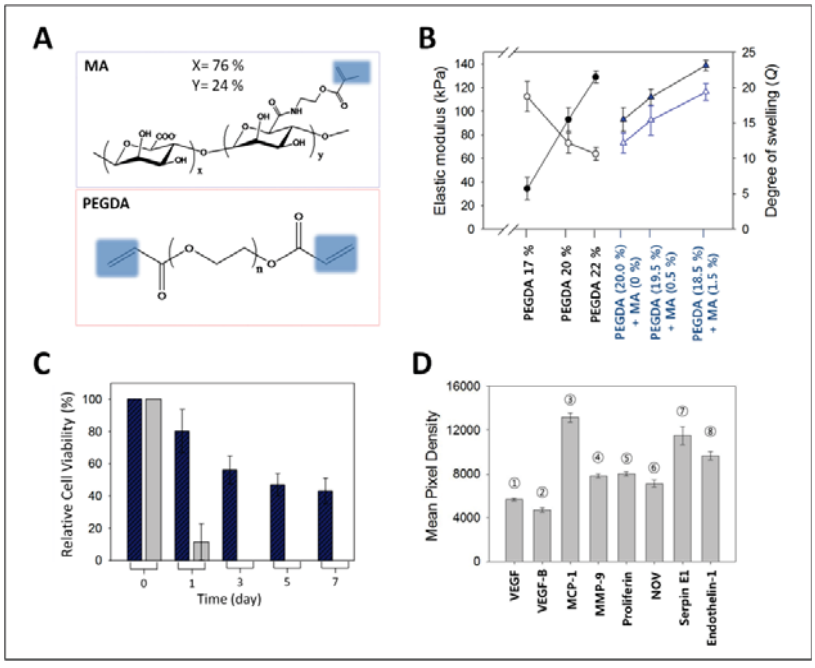

Aim 3: To demonstrate blood vessel patterning using microvascular stamps implanted on chick chorioallantoic membranes (CAMs)

By combining the SLA technology with this novel hydrogel system, we created a microvascular patch that releases multiple proangiogenic factors along its predefined patterns to spatially organize neovessels (Fig. 3A). Microchannels with controlled spacing were introduced into the PEGDA-MA hydrogels with the goal of driving neovessel growth along its circular pattern (Fig. 3B). Fibroblast-encapsulated hydrogels were implanted onto CAM membranes to validate whether the microchannel geometry of the hydrogels affected neovessel formation (Fig. 3C). We hypothesized that the neovessel growth direction could be controlled by increasing the flux of cell-secreted proangiogenic factors through the microchannel wall, with the intent to localize neovessels within the microchannel lumen. According to Fick's law of diffusion, we determined that, for a 200 μm thick hydrogel, the diameter (d) of the microchannels should be less than 800 μm in order for the flux through the microchannel wall to be greater than the flux through the bottom of the patch with the same diameter. Based on this prediction, microchannels with d = 300 , 500, and 1000 μm were fabricated to test this hypothesis. Remarkably, implantation of the PEGDA-MA hydrogel containing microchannels with d = 300 (Fig. 3D) and 500 μm (Fig. 3E) stimulated the growth of neovessels along its circular pattern, while microchannels with d = 1000 μm (Fig. 3F) did not.

Figure 3

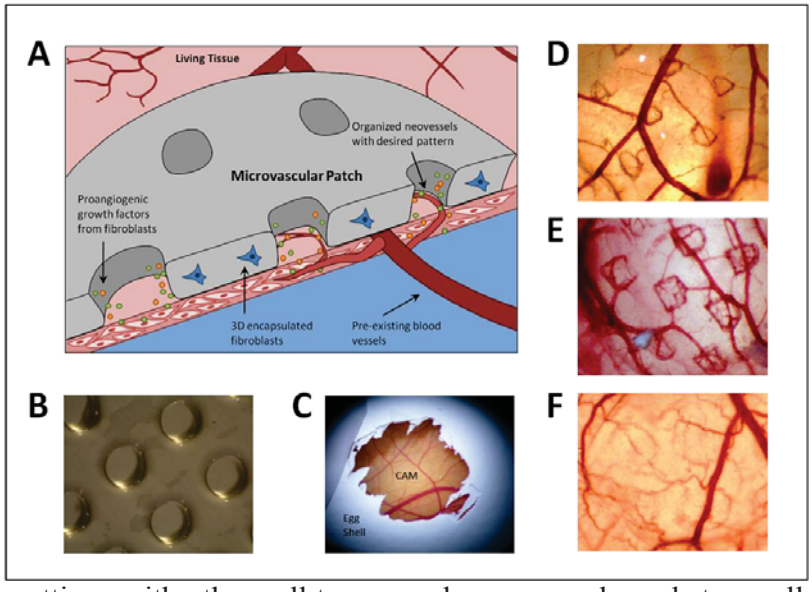

Overall, this study demonstrated that the bulk properties of the cardiac patch played a critical role in activating cellular expression of proangiogenic factors and the geometry of the microchannel patterns regulated the local distribution of proangiogenic factors on the implant site. These two material variables were orchestrated to spatially organize neovessels into the predefined pattern of the cardiac patch. This patch can be readily modified for clinical settings with other cell types, such as mesenchymal stem cells, which also endogenously express multiple proangiogenic growth factors. In the near future, we plan to incorporate this cardiac patch into an *in vivo* myocardial infarct animal model to see if it can stimulate the growth of spatially organized neovessels at the site of injury, thereby preventing scarring and deterioration of the heart.

Research Group: Taher Saif

Period Oct'10 to Sept.30, 2011

I. SUMMARY OF WORK

We have researched in three directions to study the: **a)** effect of myocyte network on local and global contraction performance, **b)** behavior of myocyte on thin pdms-membranes and **c)** effect of myocyte alignment on topographically patterned substrates. The network studies have shown that myocytes avoid debris during culture evolution. The connections between myocytes via fibroblast stop after optimizing the number of connections and local density. Large amplitudes and high contraction rates are typical properties of optimized networking. Myocytes on elastic pdms membranes have shown smaller contraction and lower rate than myocytes on polystyrene substrates during the first three days of cell culture. However, this scenario inverts with culture evolution. After 27 days, myocytes on membranes contracts with amplitude of 7 μm and rate of 30 bpm compared to 2 μm and 6 bpm for myocytes on polystyrene. Interestingly, myocytes on thin elastic membranes survived 103 days compared to 34 days on hard substrates. These results indicate that adjusting the myocyte environment by choosing the correct mechanical properties may become crucial for myocyte survival in cell regeneration therapies. Myocyte alignment along parallel topographical patterns expedited the synchronization effects but did not significantly change the dynamical performance in terms of amplitude and rate. All studies above were made for different segments of the hearts and regional differences are mentioned below.

II. INTRODUCTION

The goals of the Saif's subgroup were to assess the intrinsic properties of myocyte dynamical behavior *in vitro* and to control the myocyte evolution for engineered designed substrates. Cell-injection therapies have been used to create new tissue, however cell death and limited proliferation after transplantation hinder the formation of new myocardium[1]. A significant challenge remains in identifying the optimal cell type for integration into the heart to promote cardiac myogenesis[2,3]. The heterogeneity of cell types and their function in the heart is a source of the underlying complexity in cardiac regeneration therapies. Previous investigations have shown that myocytes from different regions of the heart are different in terms of sarcomere length[4] and dynamical properties[5]. In this part of the project is studied how the myocyte-network develops in flat and topographically patterned substrates. An ultra-thin PDMS-membrane is proposed as potential substrate to promote myocyte dynamic. A record of myocyte age was obtained by observation of dynamical active myocytes even after 104 days of cell culture.

III. BODY

1. Myocyte-network

Network formation was observed from images collected using phase contrast optics on an Olympus IX81 microscope using a 20X objective and videos recorded at 72 frames per second. Image processing was done via MATLAB (The MathWorks, Natick, MA) and statistical analysis was computed in Origin (OriginLab Corporation, Northhamption, MA).The myocyte contraction was tracked via the previous introduced Displacement Myocytogram (DMG)[6] and displayed as a scalar field of rate and amplitude. One myocyte culture is extracted from one segment of one heart (apex, ventricle or atrium) and cultured in separate polystyrene petri dishes. Multiwell plate with grids purchased from Pioneer Scientific (Code: PSMP6-G) were used to re-find the same location at different days.

Figure 1a-c display a typical network formation for myocytes from atrium at the day2, day6 and day10, for a, b and c, respectively. The size of one image is (408 x 309) μm and the bar in each image corresponds to 100 μm. These images are only one example of how myocyte-network forms and stops. The complete experiment and following data analysis is based on the video-microscopy recorded every day at three independent regions on the petri-dish for 6 independent hearts and the complete frame of interest is four times larger (=816x480 μm) than one image displayed below. The use of such large area is a necessary condition to assess global properties. A re-finding procedure was tested prior to this study. The deviation from the expected match for test images was less than 5 μm in 408 μm. The accuracy of 98.75% enables the exclusion of re-finding error in later discussions. A total amount of 36 videos were recorded daily for 3 weeks (=6 hearts x 3 segments x 3 regions on petri-dish).

At early stage of cell culture (=day2) the amplitude of contraction is small and the rate is low for atrial myocytes (Figure 1d,g). Myocytes from the ventricle do not behave in the same way. The amplitude and rate at day 2 displayed in Figure 2d,g by the scalar fields is significantly different than the values for atrial myocytes. The amplitude increases for both type of cells with evolution of the network, but they keep their relative difference as shown in Figure1e and Figure2e. Interestingly, the rate of atrial myocytes does not change with time but the scalar fields for ventricle cells display that amplitude and rate is increased Figure 2d,e, g,h. At day10, the amplitude of atrial myocytes does not show relevant differences compared to day6 (Figure 1e,f). However, this statement is not valid for the rate which increases from values of 10 to 25 (bpm) (Figure 1h,i). The opposite is observed in case of ventricle myocytes for the evolution during this period of time. Large amplitudes are rather localized (Figure 2f) at particular regions and the rate generally decreases (Figure 2i) at day10.

The observations above are based on the global properties of the network from different types of myocytes obtained from the analysis of all data recorded in this experiment. Local effects can be observed depending on the type of networking. Due to unknown reason, atrial myocytes have typically larger amount of tissue fragments and debris. Their network is dense from early stages but not necessarily dense from contractile cells. This property is suggested as a reason for the very different behavior between atrial and ventricle myocyte during the first week of culture.

After one week, a monolayer build of fibroblast covers the entire area and provides similar substrate conditions for both types of cells resulting in similar contraction amplitudes. A change of amplitude does not implicate on a change of rate. The results show that the amount of myocyte-fibroblast-myocyte connections plays fundamental role for the contraction rate and the sequence of movies recorded for this study reveals that the density of contractile cells is higher for ventricle than for atrial myocytes. It is suggested that the same tissue fragments and debris from early stage of culture sticks to the substrates and becomes a source of dynamical resistance in later evolution. This argument is consistent with the observations of morphological differences between atrial and ventricle myocytes[7,8].

Figure 1.

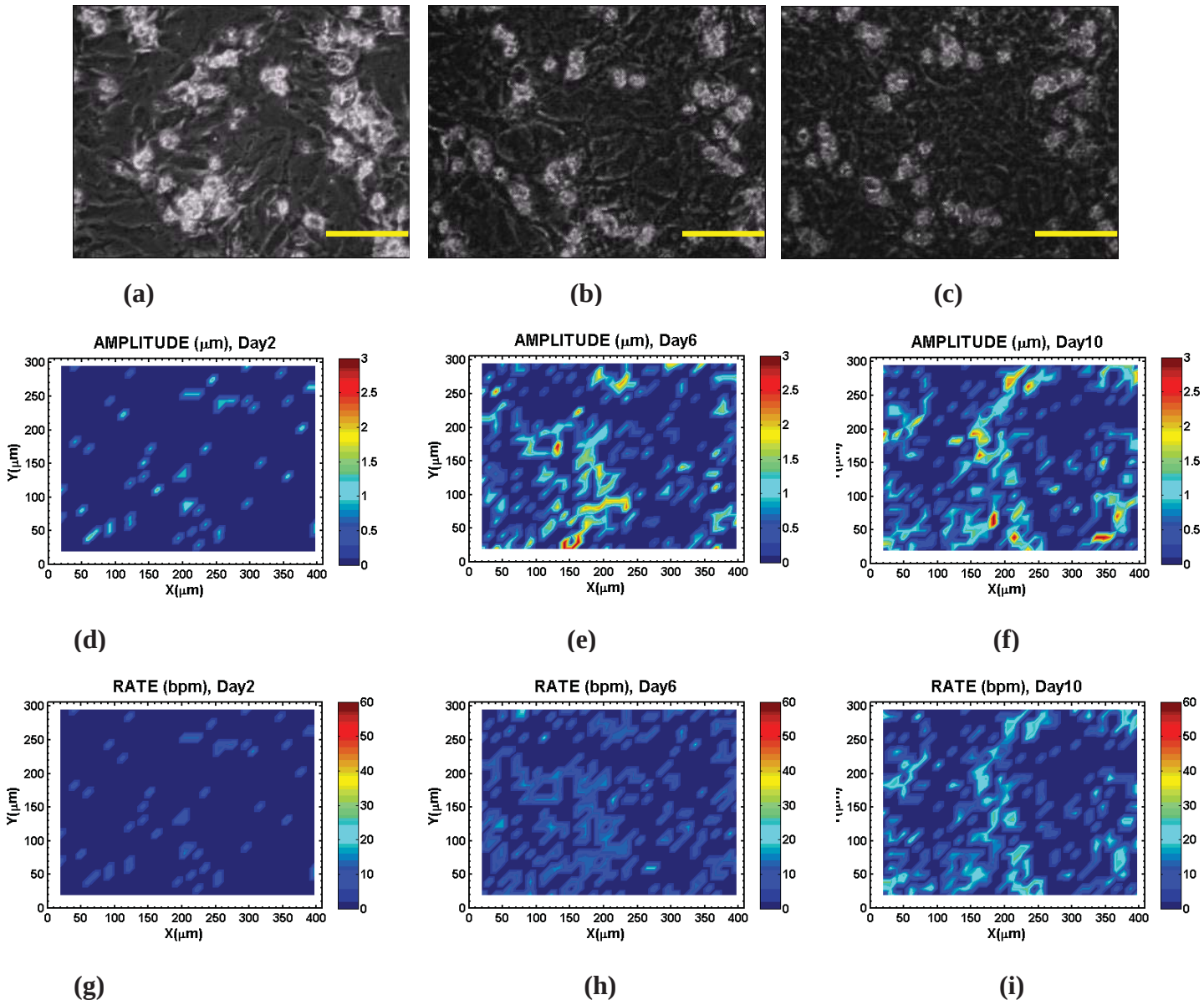

Figure 2

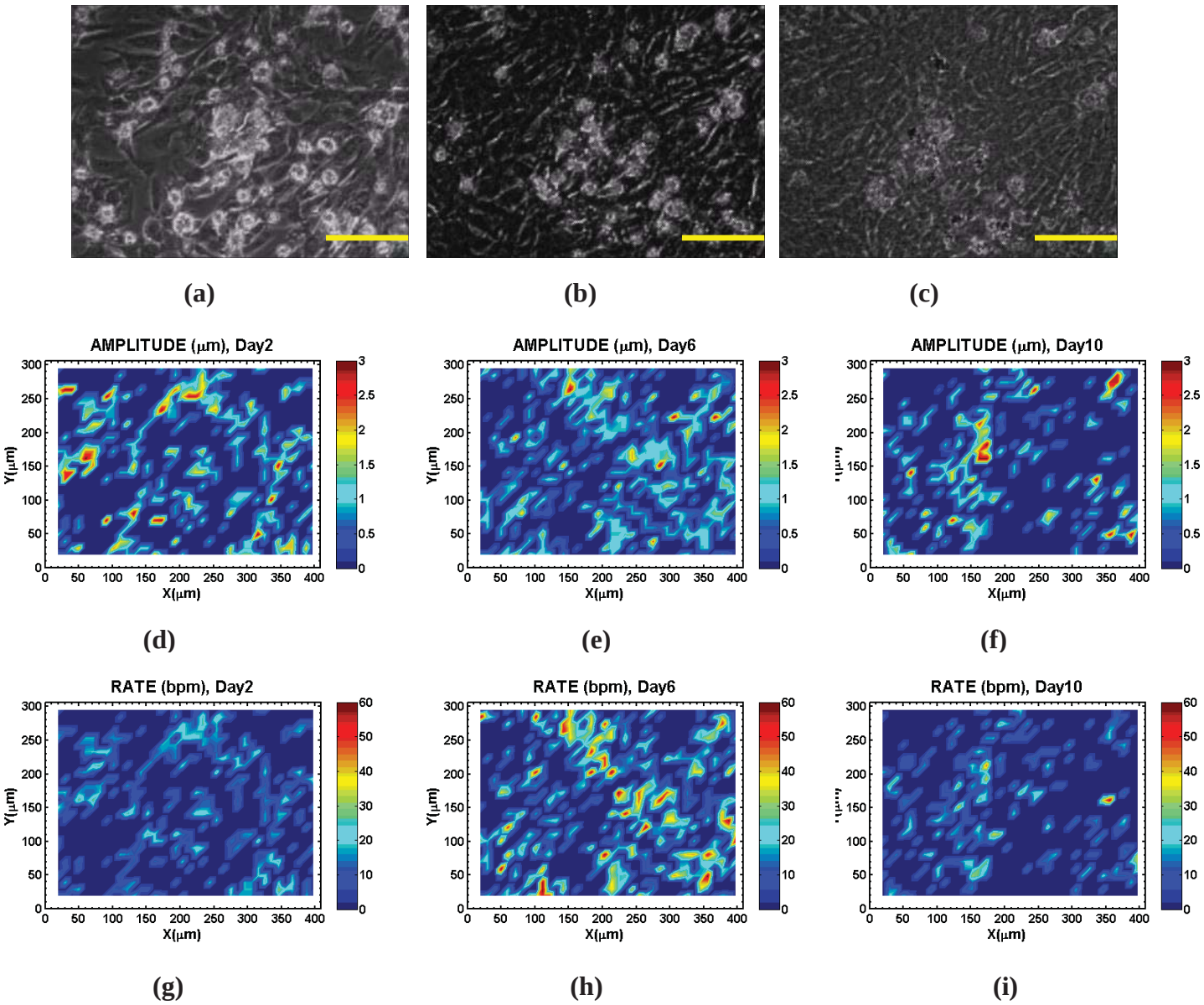

2 Effect of myocyte alignment on topographically patterned substrates

In this section we studied how atrial and ventricle myocytes respond to topographically patterned pdms substrates. Liquid PDMS of 1:10 ratio (cross-link:polymer) was poured on the top of an electronic circuit (Figure 3 below) and removed after curing at 75°C.

Figure 3

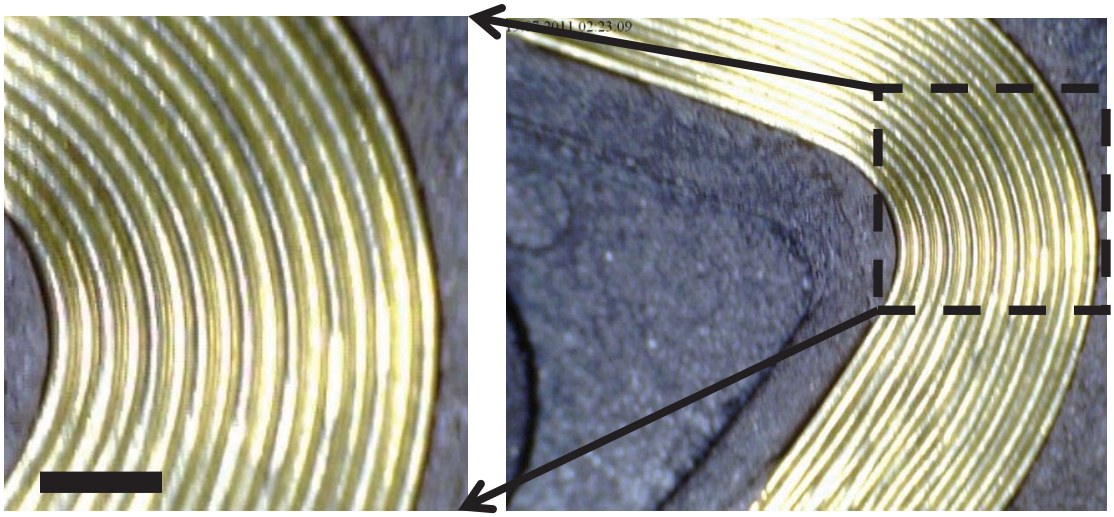

The bar in the left image corresponds to 300 μm. The lateral separation between the lines is 175±15 μm and the depth between the lines is approximately 200 μm. The substrates were treated with fibronectin and the two types of myocytes were cultured on these surfaces for 7days. Figure 4a-c displays series of images to reconstruct the global view of how atrial myocytes adhered to the surfaces.

Figure 4

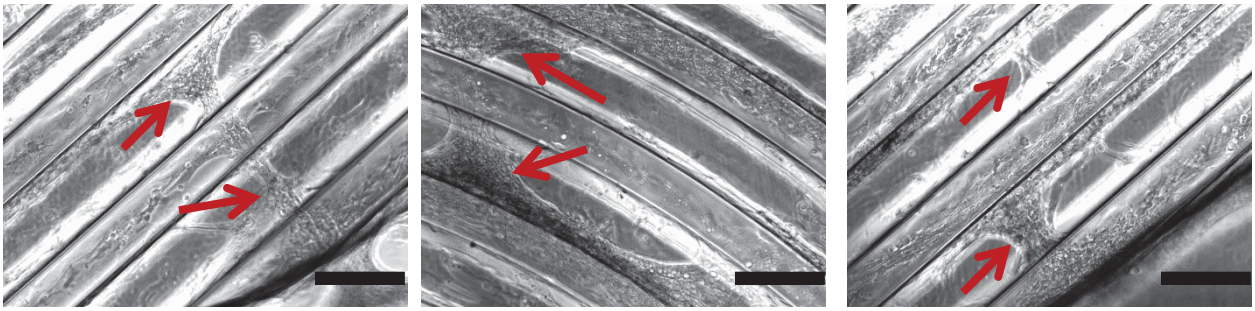

(a) **(b)** **(c)**

The black bar corresponds to 200 μm and the red arrows indicate the position of the contractile myocytes. Interestingly, these myocytes do not necessarily follow the alignment and curve of the substrate but bridges the 150 μm gap between two lines. The typical contraction property of these myocytes is displayed in the DMG below (Figure 6a).

Ventricle myocytes again behaves different in this new scenario as it is shown in Figure 5:

Figure 5

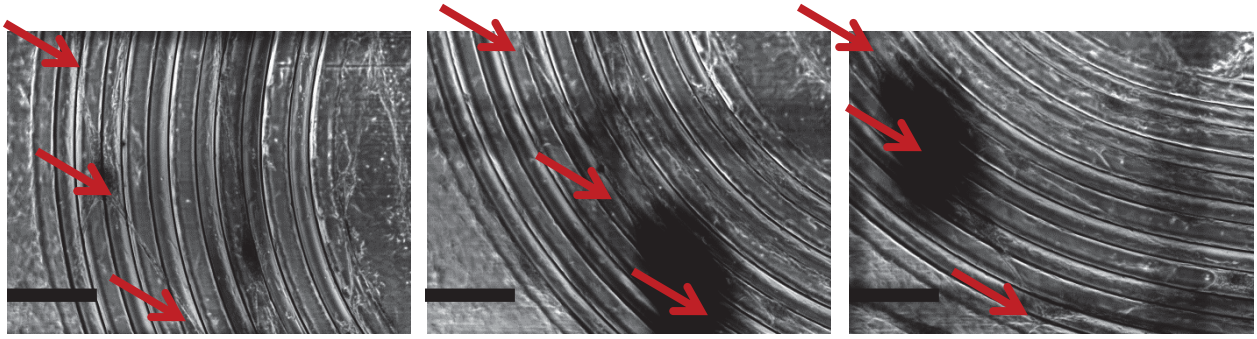

(a) **(b)** **(c)**

As above, the black bar corresponds to 200 µm and the red arrows indicate the position of the contractile myocytes. Multiple myocytes are connected through thin 'ligaments' following the curve and approaching a final length up to 2mm. A segment of this connection is demonstrated in Figures 5a-c. The first connection to the substrate is seen in top left of Figure 5a. The direction of the arrow indicates to direction of view. Therefore, Figure 5b is the continuation of Figure 5a but slightly moved to the right following the curve and likewise it proceeds in Figure 5c. The ventricle myocytes contract synchronous and the typical behavior is shown by the DMG below (Figure 6b):

Figure 6

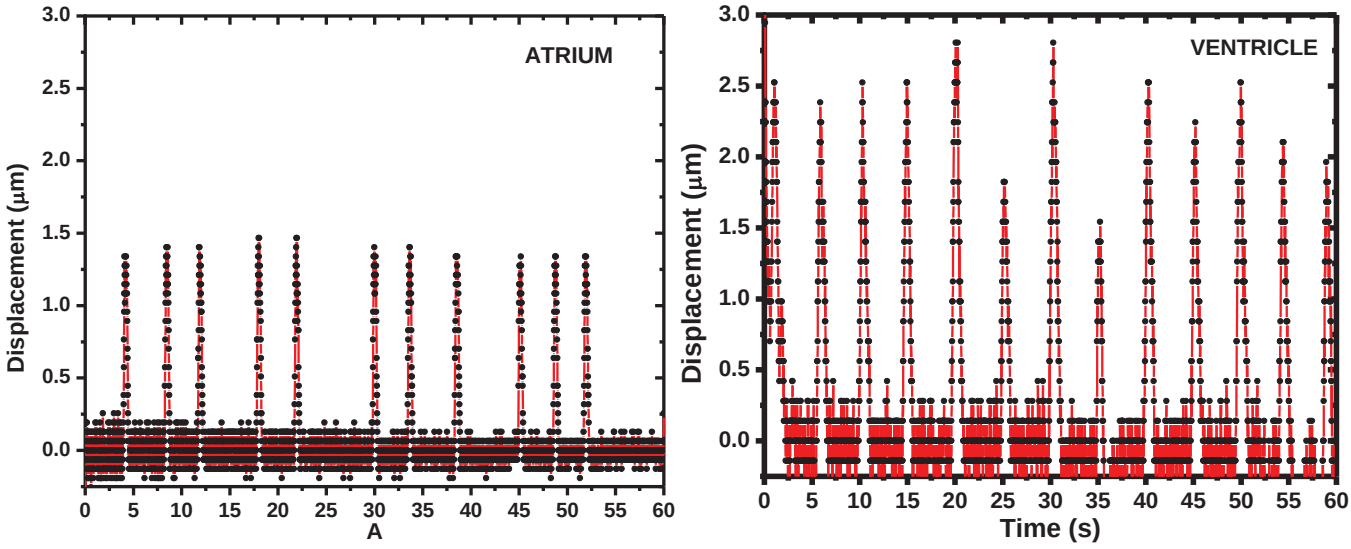

(a) **(b)**

Contraction rate and amplitude are following similar behavior as discussed above for flat substrates at the same culture-age, however, the long myoycte-myocyte connection observed on the patterned substrate is a new and revealed new differences between these two types of myocytes. A systematic investigation of age on patterned substrates is necessary for rigorous understanding of the differences due to the combined effect of different myocyte types and different topographically patterned substrates.

3. Myocyte evolution on ultra-thin elastic pdms-membranes

A ultra-thin PDMS membrane of 10 µm thickness and 20 mm for width x height is constructed in a way that myocytes can be cultured from both sides of the membrane as displayed in the schematic diagram below (Figure 7).

Figure 7

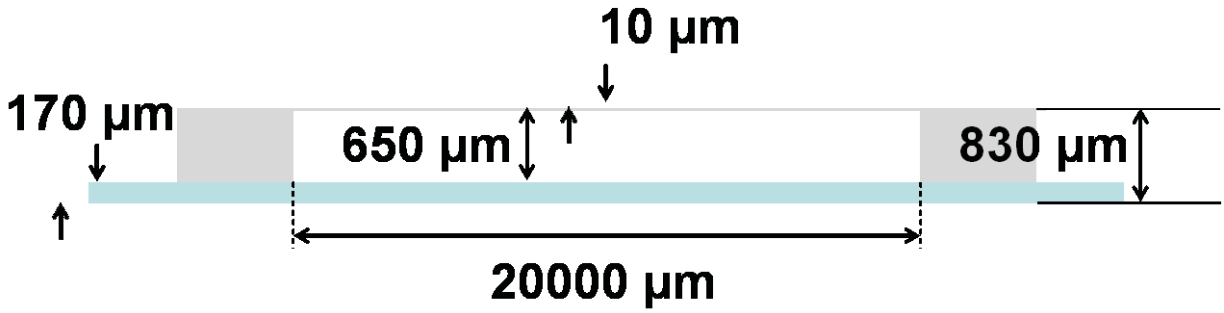

The device is designed to study purely mechanical communication between myocytes. With a 400 µm needle the myocytes suspension in inserted in the chamber and cultured from the bottom side. Later, the membrane is turned upside down and myocytes are cultured on the top of the membrane. The image below (Figure 8) shows a monolayer of ventricle myocytes only on the top of the membrane:

Figure 8

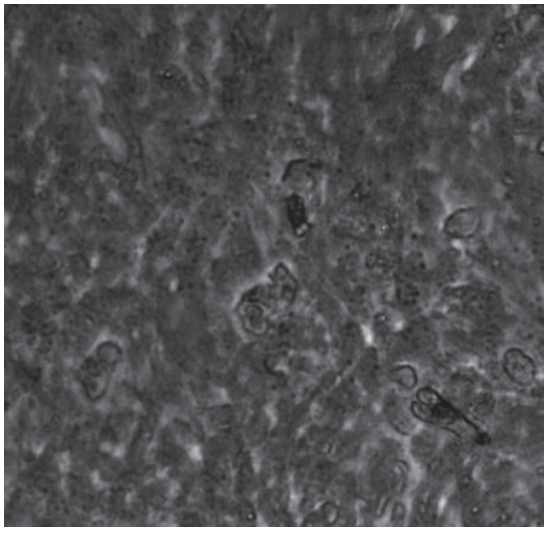

The myocytes were cultured for 104 days and were still contracting with rate of 22 bpm and amplitude of 5 μm. This positive surprising result breaks the record of 21 days of myocyte-age in vitro reported in earlier studies [9] and 34 days in the present study on polystyrene. This device promotes also potential investigation of induced mechanical oscillation and effect of gradient stiffness along the membrane.

IV. KEY RESEARCH ACCOMPLISHMENTS

- Myocyte-network also depends on the region the cells are extracted from the heart.
- The local formation of myocyte-fibroblast-myocyte-connection is limited by the distance between myocytes and the local density of cells including tissue fragments and debris.
- Optimized networking is characterized by largest amplitude and highest contraction rate compared to their neighborhood
- Ultra-thin PDMS-membranes favors myocyte dynamic after the 4th day of cell culture
- The culture age of myocytes on membranes is extended to 104 days (new record) compared to 34 days observed in this study and 21 in earlier investigation[9]
- Myocyte alignment via topographically structured substrates contributes to earlier synchronization as compared to non-aligned cells cultured on flat surfaces.

V. REPORTABLE OUTCOMES (papers submitted and in preparation)

- Cardiac myocytes' dynamic contractile behaviour differs depending on heart segment. **Full Article** submitted to Biochemical and Biophysical Research Communications
- A vector field analysis of contraction from atrial, ventricle and apex myocytes in-vitro. **Full Article** submitted to Biotechnology and Bioengineering
- Mapping myocytes contraction via digital correlation analysis: A new method for quantification of dynamical fields with sub pixel accuracy. **Full Article** submitted to Cytometry Part A
- Effect of myocyte networking on local and global stability of myocyte culture (Paper in preparation)
- Ultra-thin PDMS-membrane improve myocyte culture age (Paper in preparation)

VI. CONCLUSION

The dynamic of myocyte network and its effect on its own evolution has been observed for the first time, (to our knowledge), revealing that the global myocyte dynamic is severely affected by local effects such as resistance to motion provoked by sticky debris and tissue fragments on the substrates. Alignment of myocytes on patterned substrates is not obvious and cannot be anticipated because it depends on the substrate but and also on the type of myocyte. A rigorous investigation is needed to clarify this question. For instance, the current results show the tendency of ventricle myocytes to align and to build up long connections up to 2 mm but this did not occur for atrial myocytes. The experiment and results of long living myocytes on PDMS

membrane motivates new investigations on the effect of mechanical environment on myocytes using this device. Understanding why myocytes die *in vitro* studies can be fundamental to improve cell regeneration *in vivo*.

VII. REFERENCES

[1] C.E. Murry, Cell-based cardiac repair reflections at the 10-year point, Circulation 112 (2005) 3174-3183.

[2] K.R. Chien, I.J. Domian, K.K. Parker, Cardiogenesis and the Complex Biology of Regenerative Cardiovascular Medicine, Science 322 (2008) 1494-1497.

[3] A. Soto-Gutierrez, H. Yagi, B.E. Uygun, N. Navarro-Alvarez, K. Uygun, N. Kobayashi, Y.G. Yang, M.L. Yarmush, Cell delivery: From cell transplantation to organ engineering, Cell Transplantation 19 (2010) 655-665.

[4] M.M. Laks, M.J. Nisenson, H.J. Swan, Myocardial cell and sarcomere lengths in the normal dog heart, Circulation Research 21 (1967) 671-678.

[5] E.J. DeSouza, W. Ahmed, V. Chan, R. Bahir, T.M. Saif, Cardiac myocytes' dynamic contractile behavior differs depending on heart segment., Biochemical and Biophysical Research Communications Submitted (2011).

[6] E.J.D. Souza, T.M. Saif, Mapping myocytes contraction via digital correlation analysis: A new method for quantification of dynamical fields with sub pixel accuracy, Cytometry Part A Submitted (2011).

[7] M.J. Legato, The myocardial cell: new concepts for the clinical cardiologist, Circulation 45 (1972) 731-735.

[8] M.J. Legato, Ultrastructure of the atrial, ventricular, and Purkinje cell, with special reference to the genesis of arrhythmias, Circulation 47 (1973) 178-189.

[9] H. Orita, Modulation of cardiac myocyte beating rate and hypertrophy by cardiac fibroblasts isolated from neonatal rat ventricle, Japanese Circulation Journal 57 (1993) 912-920.

Research Group: Larry Schook

Period Aug '10 to Sept '11

Year 3

- To demonstrate and characterize the capability of using SL to design and generate complex 3-D tissue with tunable architecture
- Demonstrate improved cardiac tissue function in hydrogels with properties optimized via in vitro cell studies

I. Summary of Work

In order to test hydrogel constructs *in vivo* we have developed a mouse myocardial infarction model. Using this model we have tested the creation, placement, and adhesion of patterned hydrogel heart patches.

II. Introduction

The goals for the Schook group were to develop an in vivo model capable of testing practical applications for hydrogel heart patches. The mouse model was chosen for initial testing due its' relative simplicity and widespread use in testing new cardiac materials and methods.

III. Body

Patch transfer onto mouse hearts: Hydrogel patches approximately 200-300□m thick with a diameter of 4mm generated by SL were transferred to mouse cadaver hearts to establish techniques for transferring patches in the in vivo model. A thoracotomy is performed to expose the heart and the patch is transferred to the heart surface (Figure 1A). Patches were also applied to the heart surface of living animals under anesthesia. Hydrostatic adhesion was sufficient to hold the patches in place on hearts beating at approximately 180 beats per minute.(Figure 1B) but not after chest closure and evacuation (Figure 1C).

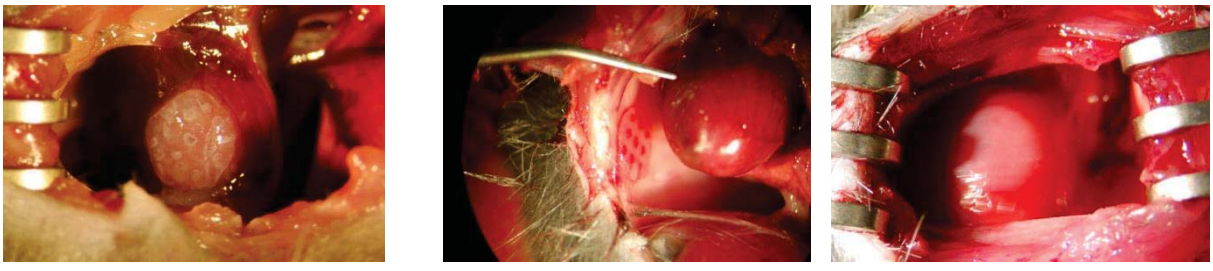

A B C

Figure 1. Hydrogel patches are applied to the surface of (A) cadaver and (B) living mouse hearts. The image in (B) is blurred due to the rapid heart rate. (C) After chest closure and evacuation, transferred patches do not remain on heart surface.

Improved mouse thoracotomy: In order to improve mouse survival during thoracotomy additional training in mouse cardiac biology and cardiology techniques was received at Jackson Laboratories in Bar Harbor Maine during a weeklong workshop entitled "Comprehensive Approaches to the in vivo Assessment of Cardiovascular Function". Echocardiograph measurements and mouse heart physiology were prominent classes and training sessions of the workshop. The full myocardial infarction procedure, including intubation and thoracotomy, was also demonstrated. Based on suggestions given during the workshop, the thoracotomy procedure was altered from a transverse thoracotomy across the 3rd to 5th ribs to an intercostal thoracotomy between the 3rd and 4th ribs to improve survival rates (Figure 2). Current thoracotomy survival rate is above 90%.

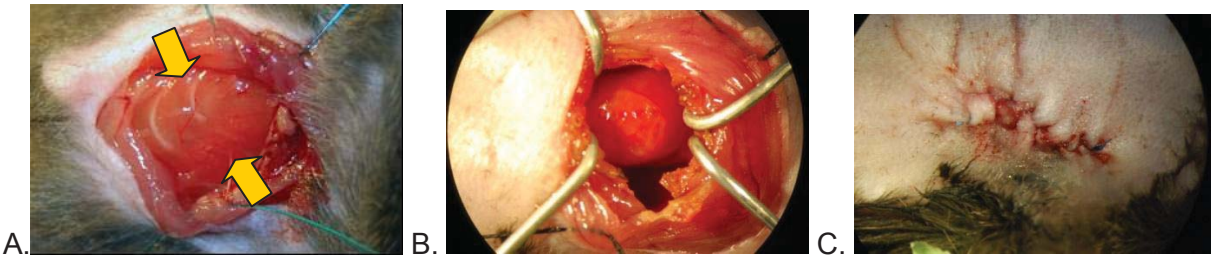

Figure 2. Intercostal thoracotomy improves survival rates. (A) The ribs are exposed by retracting the muscle layers and the intercostal space between the 3rd and 4th ribs is indicated by yellow arrows. (B) The heart is exposed after rib retraction allowing for cardiac patch application. (C) Improved closure is achieved with intercostal thoracotomy.

Adhesive testing: Using an intercostal thoracotomy between the 3rd and 4th ribs, two new methods of increasing hydrogel adhesion were tested. Patch retention on the heart surface is poor for hydrogel only constructs. Addition of collagen incorporated into the hydrogel scaffold resulted in only minimal improvement. Next, a glutaraldehyde-BSA surgical glue was used to increase patch adhesion to the heart surface. Glutaraldhyde glue was compatible with the hydrogel patch and increased initial adhesion to the heart surface. Longer-term adhesion (1 hour with chest cavity closed and evacuated) was unsuccessful.

New patch design: To increase adhesion of patches and control adhesive placement, a new patch design was formulated by the Kong group. The active adhesive unit from Mussel Adhesive Protein (MAP) is incorporated into an adhesive layer on one side of the hydrogel patches using SLA (Figure 3). The adhesive dyhydroxyphenyl group is incorporated into the heart-proximal side of the hydrogel patch allowing for directional, controlled adhesion.

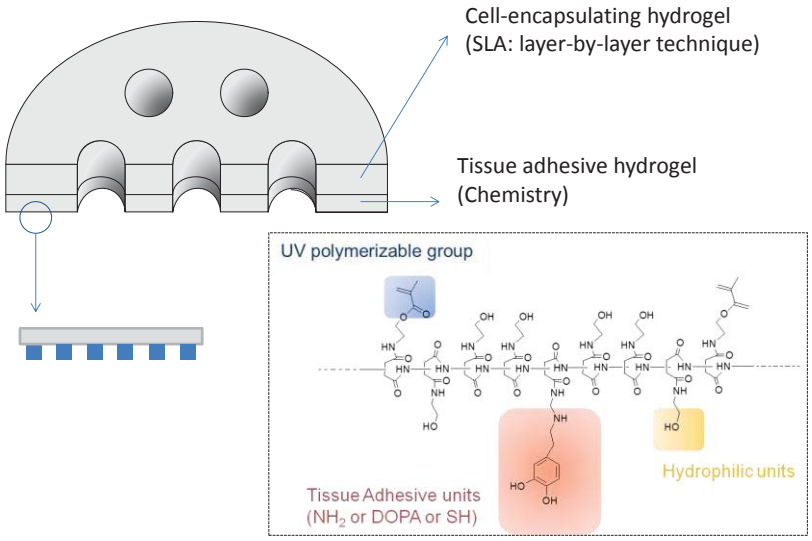

Figure 3. Adhesive patch concept from Kong Group.

Infarction Studies: Limited 14-day infarction studies have begun. Therapeutic patches will be used in this model to test efficacy. A single suture is placed in the left anterior descending (LAD) artery of the mouse to block blood flow. Mice are sutured closed, revived, and monitored for an additional 14 days. After euthanization the heart is removed and the damage is assessed indicates the initial stages of scar formation. (Figure 4).

A B

Figure 4. A suture is placed in the LAD to create myocardial infarction. After 48 hours, animals are euthanized and hearts removed for analysis. White patch below suture indicates the initial stages of scar formation.

IV. Key Research Accomplishments

- Improved mouse myocardial infarction model
- Design and initial testing of hydrogel heart patch
- Design and initial testing of adhesion formulations

V. Reportable Outcomes

Molly Melhem, Tor Jensen, Jae Hyun Jeong, Vincent Chan, Rashid Bashir, Hyunjoon Kong, Lawrence Schook. A Cardiac Patch for Delivering Therapeutic Stem Cells to the Heart Following Myocardial Infarction. University of Illinois, Chicago. Third Stem Cell and Regenerative Medicine Symposium. May 20, 2011

VI. Conclusion

With the current *in vivo* model we will perfect the production and application of hydrogel-based heart patches generated by SLA. Both encapsulated cells and drugs will be tested for their ability to reduce cardiac damage following myocardial infarction. Initial experiments in the mouse model will allow for the scaling of similar patches in larger, more relevant animal models in the future. Current adhesive patch designs will also have direct relevance to other applications in soft tissues requiring prolonged exposure of target tissues to cells and/or drugs stabilized by hydrogel matrices.

Research Group: Hyunjoon Kong

Period Aug'10 to Aug'11

I. SUMMARY OF WORK

Kong's group's goal was to build a microvascular stamp using 3D stereo-lithographic technology to guide and pattern blood vessel formation.

Aim 1: To adapt the 3D stereo-lithographic apparatus for biological components (*i.e.* living cells, photopolymerizable hydrogels, and signaling proteins)

Aim 2: To develop a novel photo-polymerizable hydrogel matrix that decouples elastic modulus and swelling ratio

Aim 3: To demonstrate blood vessel patterning using microvascular stamps implanted on chick chorioallantoic membranes (CAMs)

II. INTRODUCTION:

Neovessels play a critical role in homeostasis, regeneration, and pathogenesis of tissues and organs, and their spatial organization is a major factor in influencing vascular function. Therefore, successful treatments of wounds, ischemic tissue, and tissue defects greatly rely on the ability to control the number, size, spacing, and maturity of blood vessels regenerated within a target tissue. However, technologies to control the spatial organization of mature neovessels in vivo over physiologically-relevant length scales are still lacking. Here, we present a study of a 'living' microvascular stamp that releases multiple angiogenic factors and subsequently creates neovessels with the same pattern as that engraved in the stamp.

Using stereolithography, we developed a microvascular stamp that releases multiple angiogenic growth factors and guides the formation of neovessels within patterns defined by the stamp. The stamp consists of living cells that secrete angiogenic growth factors, an engineered hydrogel matrix that promotes cellular expression of angiogenic growth factors, and a three-dimensional (3D) geometry that localizes the angiogenic growth factors within the patterns. The potential impact is the development of functioning vasculature that supports biological components *in vitro* (*i.e.* cell clusters in a bio-bot) or regeneration of chronic diseases or ischemic wounds *in vivo*.

III. BODY:

A. Progress toward Objectives and Significant Achievements:

Aim 1: To adapt the 3D stereo-lithographic apparatus for biological components

First, we introduced the capabilities of the SLA technology. The SLA is a computer-aided design (CAD) based rapid prototyping system that provides excellent spatial control over the matrix

architecture (Fig. 1A). The core concept is to use a UV laser to polymerize a liquid photopolymer by repetitive deposition and processing of individual layers into a desired 3D pattern. The SLA is both reproducible and high-throughput. In our recent work, we established four key capabilities of the SLA. It can be used (1) to pattern tissue-like hydrogels into complex 3D constructs (Fig. 1B), (2) to encapsulate cells into these hydrogel constructs (Fig. 1C), (3) to incorporate multiple materials, cell types, and proteins into distinct layers on the same construct (Fig. 1D), and (4) to maintain cell viability, spreading, and proliferation over long periods in culture (Fig. 1E, 1F).

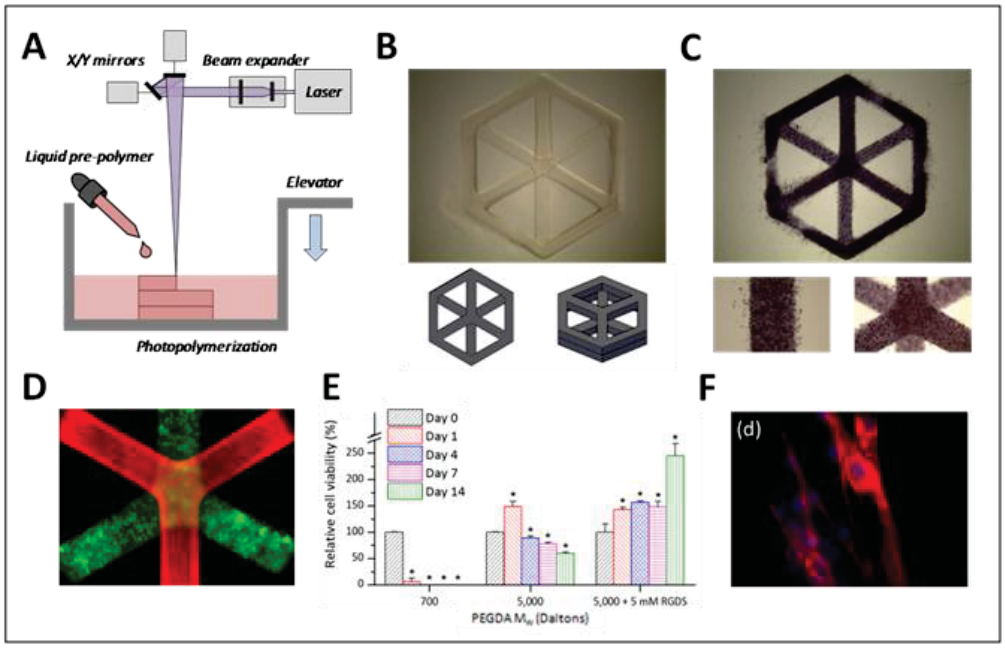

Aim 2: To develop a novel photopolymerizable hydrogel matrix that decouples elastic modulus and swelling ratio

The dream to manufacture clinically-viable tissues and organs jump-started the field of tissue engineering and regenerative medicine in the 1990s to accommodate for the shortage of organ donors. Today, the shortage still exists and the development of tissue equivalents has stalled. This is partly due to the lack of advanced vascularization strategies for controlling the direction and spacing of neovessel growth. Metabolically-demanding tissues such as those in the heart, brain, and liver need capillaries within 500 μm of each other in order to have sufficient oxygen tension. Therefore, vascularization is a central component in the design of any approach to tissue engineering. The aim of our work is to focus on enabling technologies to develop a clinically-viable vascularization method through the combined use of a 3D stereo-lithographic (SLA) patterning technique and a novel growth factor-cell-matrix combination therapy.

We developed a novel poly(ethylene glycol) diacrylate (PEGDA) and methacrylic alginate (MA) hydrogel matrix (Fig. 2A) capable of stimulating encapsulated cells to release multiple proangiogenic growth factors, while maintaining structural integrity at the implant site. The elastic modulus and swelling ratio were tuned to prepare a rigid, yet permeable PEGDA-MA hydrogel so that the cell-encapsulated hydrogel would not only remain stable, but also support cellular expression of proangiogenic factors (Fig. 2B). The role of MA was to reverse the typical inverse relationship between stiffness and bulk permeability that conventional hydrogel systems have. The increase in the bulk permeability of the PEGDA-MA hydrogel translated into improved cell viability compared to PEGDA only (Fig. 2C). Subsequently, fibroblasts that are known to endogenously express proangiogenic factors were encapsulated into the PEGDA-MA hydrogels. As revealed by microarray analysis, fibroblasts encapsulated within PEGDA-MA hydrogels expressed large amounts of multiple proangiogenic factors (Fig. 2D).

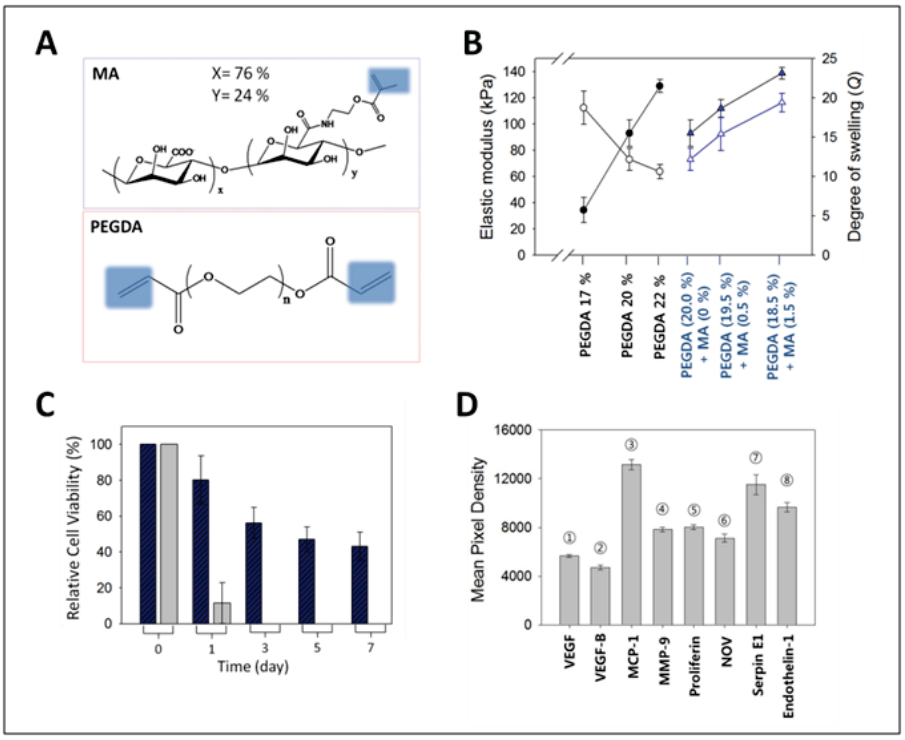

Aim 3: To demonstrate blood vessel patterning using microvascular stamps implanted on chick chorioallantoic membranes (CAMs)

By combining the SLA technology with this novel hydrogel system, we created a microvascular patch that releases multiple proangiogenic factors along its predefined patterns to spatially organize neovessels (Fig. 3A). Microchannels with controlled spacing were introduced into the PEGDA-MA hydrogels with the goal of driving neovessel growth along its circular pattern (Fig. 3B). Fibroblast-encapsulated hydrogels were implanted onto CAM membranes to validate whether the microchannel geometry of the hydrogels affected neovessel formation (Fig. 3C). We hypothesized that the neovessel growth direction could be

controlled by increasing the flux of cell-secreted proangiogenic factors through the microchannel wall, with the intent to localize neovessels within the microchannel lumen. According to Fick's law of diffusion, we determined that, for a 200 μm thick hydrogel, the diameter (d) of the microchannels should be less than 800 μm in order for the flux through the microchannel wall to be greater than the flux through the bottom of the patch with the same diameter. Based on this prediction, microchannels with d = 300 , 500, and 1000 μm were fabricated to test this hypothesis. Remarkably, implantation of the PEGDA-MA hydrogel containing microchannels with d = 300 (Fig. 3D) and 500 μm (Fig. 3E) stimulated the growth of neovessels along its circular pattern, while microchannels with d = 1000 μm (Fig. 3F) did not.

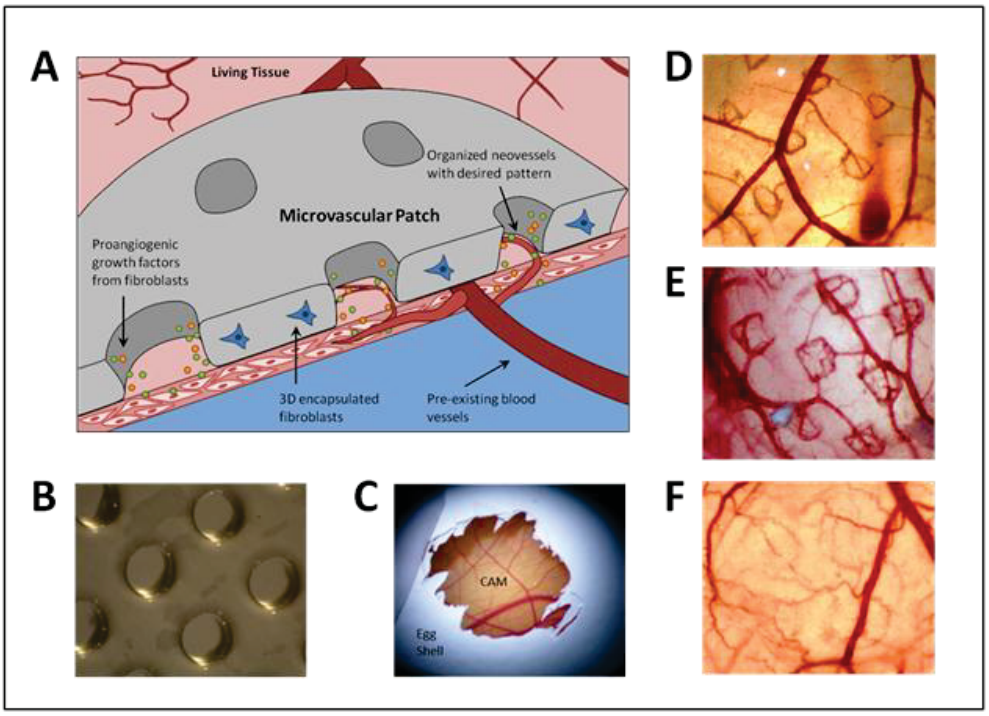

Overall, this study demonstrated that the bulk properties of the cardiac patch played a critical role in activating cellular expression of proangiogenic factors and the geometry of the microchannel patterns regulated the local distribution of proangiogenic factors on the implant site. These two material variables were orchestrated to spatially organize neovessels into the predefined pattern of the cardiac patch. This patch can be readily modified for clinical settings with other cell types, such as mesenchymal stem cells, which also endogenously express multiple proangiogenic growth factors. In the near future, we plan to incorporate this cardiac patch into an *in vivo* myocardial infarct animal model to see if it can stimulate the growth of spatially organized neovessels at the site of injury, thereby preventing scarring and deterioration of the heart.

IV. KEY RESEARCH ACCOMPLISHMENTS:

- Kong's group has synthesized bioactive, bio-degradable methacrylic alginate (MA) and demonstrated hydrogel fabrication with stereo-lithographic apparatus.
- The role of MA was to reverse the typical inverse relationship between stiffness and bulk permeability that conventional hydrogel systems have.
- Kong's group has developed a novel poly(ethylene glycol) diacrylate (PEGDA) and methacrylic alginate (MA) hydrogel matrix capable of stimulating encapsulated cells to release multiple proangiogenic growth factors, while maintaining structural integrity at the implant site.
- Kong's group has developed a method to provide excellent spatial control over the matrix architecture into the gel using a stereolithographic assembly (SLA).
- Kong's group has created a 'living' microvascular stamp that releases multiple angiogenic factors and subsequently creates neovessels with the same pattern as that engraved in the stamp.

V. REPORTABLE OUTCOMES:

List of papers published in peer-reviewed Journals

- C. Cha, S.Y. Kim, L. Cao, H. Kong, Decoupled control of stiffness and permeability with a cell-encapsulating poly(ethylene glycol) dimethacrylate hydrogel. ***Biomaterials*** (2010) 31, 4864-4871

- R.J. DeVolder, H. Kong, Three dimensionally flocculated proangiogenic microgels for neovascularization. ***Biomaterial***s (2010) 31, 6494-6501

- Y. Liang, T.W. Jensen, E.J. Roy, C. Cha, R.J. DeVolder, R.E. Kohman, B.Z. Zhang, K.B. Textor, L.A. Rund, L.B. Schook, Y.W. Tong, H. Kong, Tuning the non-equilibrium state of a drug-encapsulated poly(ethylene glycol) hydrogel for stem and progenitor cell mobilization. ***Biomaterials*** (2011) 32, 2004-2012

- J.H. Jeong, V. Chan, C. Cha, P. Zorlutuna, C. Dyck, K.J. Hsia, R. Bashir, and H. Kong., 'Living' microvascular stamp for patterning of functional neovessels; Orchestrated control of matrix property and geometry. ***Advanced Materials*** (2011) in press.

List of abstracts and presentations in related conferences

- J.H. Jeong, V. Chan, C. Cha, P. Zorlutuna, Rashid Bashir, and Hyunjoon Kong, "In situ cell encapsulation into a vascularized hydrogel matrix using a SLA." Outstanding research award in stem cell and regenerative medicine, Tissue Regenerative Symposium, March 24, 2010, Chicago, IL, USA.

- J.H. Jeong, V. Chan, C. Cha, P. Zorlutuna, R. Bashir, H. Kong, "Assembly of functional neovessels using a stereolithogrphically assembled hydrogel." 1st place poster winner on Regenerative Biology and Tissue Engineering, October 22, 2010, Institute for Genomic Biology, Champaign, IL, USA.

- J.H. Jeong, V. Chan, C. Cha, P. Zorlutuna, R. Bashir, H. Kong, "Assembly of functional neovessels using a stereolithographic hydrogel matrix." Oral presentation, American Chemical Society (ACS) National Spring Meeting, March, 2011, Anaheim, USA.

- J.H. Jeong, V. Chan, C. Cha, P. Zorlutuna, R. Bashir, H. Kong, "Assembly of functional neovessels using a stereolithographic hydrogel matrix." 2011 Society For Biomaterials (SFB) Annual meeting, April 13-16, Orlando, FL, USA.

- J.H. Jeong, V. Chan, C. Cha, P. Zorlutuna, C. Sukotjo, R. Bashir, H.Kong, "Independent control stiffness and permeability of a cell-encapsulating hydrogel for tissue engineering." Oral presentation, 2011 BMES Annual meeting, October 12-15, 2011, Hartford, USA.

- J.H. Jeong, V. Chan, C. Cha, P. Zorlutuna, R. Bashir, H. Kong, "Independent control stiffness and permeability of a cell-encapsulating hydrogel; Integration of Bio-inspired material chemistry and microfabrication." Oral presentation, 2011 AIChE Annual Meeting, October 16-21, 2011, Minneapolis, MN, USA.

VI. CONCLUSION:

Kong's group has developed a 'living' microvascular stamp that releases multiple angiogenic factors and subsequently creates neovessels with the same pattern as that engraved in the stamp. The stamp consists of live cells that secrete angiogenic factors, an engineered hydrogel matrix that promotes cellular expression of angiogenic factors, and a three-dimensional (3D) geometry that localizes the angiogenic factors within the pattern. When the stamp was implanted on a target site, it created the desired pattern of neovessels based on 3D geometry of the stamp, allowing the control of the density and spacing of blood vessels.

Overall, this study demonstrated that the bulk properties of the cardiac patch played a critical role in activating cellular expression of proangiogenic factors and the geometry of the microchannel patterns regulated the local distribution of proangiogenic factors on the implant site. These two material variables were orchestrated to spatially organize neovessels into the

predefined pattern of the cardiac patch. This patch can be readily modified for clinical settings with other cell types, such as mesenchymal stem cells, which also endogenously express multiple proangiogenic growth factors. In the near future, we plan to incorporate this cardiac patch into an *in vivo* myocardial infarct animal model to see if it can stimulate the growth of spatially organized neovessels at the site of injury, thereby preventing scarring and deterioration of the heart.

VII. REFERENCES:

(1) P. Carmeliet, R.K. Jain, *Nature* 2000, 407, 249

(2) R.J. DeVolder, H. Bae, J. Lee, H.J. Kong, *Advanced Materials* 2011, 23, 3139

(3) D-E. Discher, D-J. Mooney, P-W. Zandstra, *Science* 2009, 324, 1673

(4) M-P. Lutolf, J-A. Hubbell, *Nature Biotechnology* 2005, 23, 47

(5) E-M. Conway, D. Collen, P. Carmeliet, *Cardiovasc. Res.* 2001, 49, 507

Research Group: Brian Cunningham

Plastic-Based Distributed Feedback Laser Biosensors in Microplate Format

I. SUMMARY OF WORK

A process that combines polymer nanoreplica molding with horizontal dipping was used to fabricate large area (~3x5 inch^2) distributed feedback laser biosensors (DFBLB) on flexible plastic substrates, which were subsequently incorporated into standard format 96-well microplates. A room temperature nanoreplica molding process was used to create subwavelength periodic grating structures, while a horizontal dipping process was used to apply a ~300 nm, dye-doped polymer film. In this work, the DFBLB emission wavelength, used to characterize the device uniformity, demonstrated a coefficient of variation (CV) of 0.41% over the fabricated device area, representing a thickness standard deviation of only ~35 nm for the horizontal dipping process. The fabricated sensors were further characterized for sensitivity uniformity by measuring the bulk refractive index of the media exposed to the sensor surface and by measuring adsorption of biomolecular layers. An assay for detection of the cytokine Tumor Necrosis Factor-alpha (TNF-α) was used to demonstrate the operation of the sensor in the context of label-free detection of a disease biomarker. The demonstrated capability represents an important step towards roll-to-roll manufacturability for this biosensor that simultaneously incorporates high sensitivity with excellent wavelength shift resolution, and adaptability to the microplate format that is ubiquitous in pharmaceutical research.

II. INTRODUCTION

Goal of this investigation:

There is a continuing need to develop label-free detection methods that combine high sensitivity with high resolution for applications that include detection of low molecular weight analytes that bind to immobilized proteins, and the detection of protein analytes such as disease biomarkers that are present at low concentrations. While biosensors based upon optical resonators such as Surface Plasmon Resonance (SPR) [1-3] and Photonic Crystal (PC) surfaces [4, 5] have been commercially available for several years, and demonstrated for a wide range of applications, there has been a strong effort to improve upon their resolution performance through the implementation of resonators with more narrow resonant bandwidths (higher quality factor, as defined by $Q=\lambda 0/\Delta\lambda 0$). Whispering Gallery Mode (WGM) resonators such as microrings [6-8], liquid-core optical rings [9, 10], microspheres [11-13] and microtoroids [14, 15] are representative examples of passive high-Q resonators that have been implemented as biosensors. However, greater Q-factor is generally accompanied by reduced sensitivity, as measured by the magnitude of the wavelength shift obtained for adsorption of biomolecules. Furthermore, high Q-factor results in increased stringency for coupling light into the resonator, leading to a requirement for a precisely tunable wavelength excitation source that diminishes the applicability of high Q-factor resonators for high throughput measurements [16].

How can DFB Biosensors provide a superior screening platform?

To be useful for applications in pharmaceutical high throughput screening (HTS), a biosensor technology must combine excellent uniformity, low-cost fabrication, compatibility with automated liquid handling equipment, (for example, through incorporation into standard format microplates), robust detection instrumentation, and the ability to rapidly measure many sensors. Sensor uniformity is a key requirement for life science applications because replicate measurements are used to determine the standard deviation and coefficient of variance of assays, which in turn determines the statistical relevance of the data. Furthermore, sensor-to-sensor uniformity is of equal importance to sensitivity in the determination of the Z-factor statistic [17] used to quantify the statistical quality of HTS data.

Recently, we have demonstrated a DFBLB that represents a departure from previous optical biosensor approaches based upon passive resonators [18, 19]. The DFBLB is an active device that achieves high Q-factor through the process of stimulated emission, resulting in Q in the range 1x104 to 2x105 without a reduction in wavelength shift sensitivity. The DFB cavity is based on a second-order Bragg grating that supports a vertically emitting mode by first-order diffraction [20]. A schematic cross-sectional diagram of the DFBLB structure is shown in Figure 1(a). The dye doped SU8 layer provides both light confinement along the horizontal direction and amplification of the oscillation mode, while the TiO2 top layer contributes to spatial mode bias into the liquid medium. The DFB laser is optically excited by a frequency doubled, Q-switched Nd:YAG (yttrium aluminum garnet) laser (532 nm, 10 ns pulse width, single pulse mode), and the emission light is coupled into a spectrometer by an optical fiber oriented normal to the device surface. A representative emission spectrum is shown in Figure 1(b). We have previously demonstrated DFBLB devices that were fabricated upon glass and plastic substrates over small surface areas [18, 19], where the dye-doped polymer layer was deposited by spin coating, a process not compatible with roll-to-roll manufacturing. While the dimensions of the replica molded grating structure are highly uniform (as they are determined by the uniformity of the photolithography and etching processes used to create the Si master wafer used for nanoreplica molding), the thickness of the dye-doped polymer layer has been found to determine the uniformity of the both the DFBLB operating wavelength and the device sensitivity. Therefore, we have sought to develop alternative approaches for application of the dye-doped polymer layer, and have adopted a recently demonstrated approach known as "horizontal dipping" [21]. Horizontal dipping is compatible with roll-to-roll mass manufacturing because it is easily controlled, performed at room temperature, and does not require substrate rotation. The process parameters of the horizontal dipping process (blade height, fluid viscosity, dipping speed) can be controlled to accurately produce polymer thin films in the thickness range of ~0.2 - 3.0 μm [21, 22].

How can DFB biosensor production scale to levels appropriate for HTS?

Here, we demonstrate the extension of the nanoreplica molding and horizontal dipping process to large surface areas, enabling the fabrication of 3×5 inch2 DFBLB active areas that are suitable for incorporation into standard format microplates. We characterize both the short-range and long-range uniformity of the DFBLB operating wavelength, bulk refractive index sensitivity, and

biolayer adsorption sensitivity. We also demonstrate the use of the DFBLB microplate for performing an antibody-antigen detection assay, through a dose-response characterization of the cytokine TNF-α. The capabilities demonstrated in this work lay the foundations for the transition of this technology towards roll-to-roll manufacturing, and the ability to produce DFBLB microplates for applications in pharmaceutical screening and protein biomarker diagnostic assays.

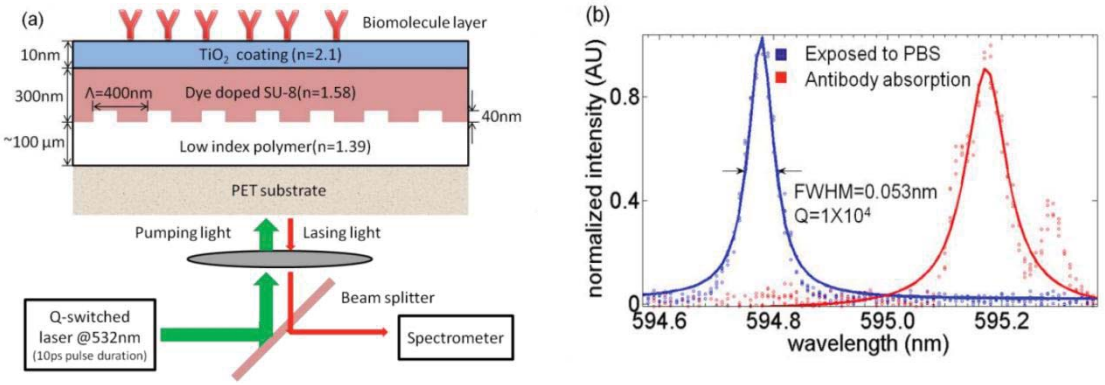

Fig. 1. (a) Schematic diagram of the DFBLB structure. The DFB laser is excited by a frequency doubled, Q-switched Nd:YAG laser (532 nm, 10 ns pulse width), and the emission light is coupled into a spectrometer by an optical fiber. (b) Lorentz fitted spectrum of DFB laser emission. The blue curve was measured when the sensor surface exposed to PBS. Full width at half maximum (FWHM) of the lasing emission is 0.053nm, resulting in quality factor=1×10^4 for typical devices reported here. The red curve shows the lasing spectra after application of the anti-TNF-α capture molecules, resulting in a peak wavelength value (PWV) shift of ~0.4nm.

III. BODY

Methods

Design and fabrication of the DFBLB by nanoreplica molding and horizontal dipping

For a second-order DFB laser, the wavelength of the emitted light (λ) is determined by the equation $m\lambda=2n_{eff}\Lambda$, where m represents the diffraction order (m=2 in this case), n_{eff} is the effective refractive index of the guidance layer, and Λ is the period of the structure. n_{eff} is determined by both the index and thickness of guidance layer. Λ is designed to be 400 nm so that the resonance wavelength is within the gain spectrum of the dye. A thin film (~300 nm) of SU-8 (n=1.58) is used as the guidance layer. As the thickness of this film varies, the n_{eff} and the emission wavelength will change correspondingly. Therefore, the standard deviation of the emission wavelength can used to infer the uniformity of the dye-doped SU8 guidance layer. The grating depth is designed to be 40 nm, as discussed in a previous publication [18].For the nanoreplica molding process, a Si "master" wafer is used as a molding template for producing the DFB grating structure. A single master wafer may be used thousands of times to produce

identical gratings. For this work, an 8-inch diameter Si wafer was patterned by nano-imprint lithography using a Molecular Imprints Imprio 50 machine [23, 24], with a 1x1 cm^2 grating imprint template. The nano-imprint lithography process was performed in a step/repeat fashion to create a 9x12 array of individual grating die, with a grating period of Λ=400 nm period, 50% duty cycle on the master wafer. After nano-imprint patterning, the grating structure was permanently transferred into the silicon by reactive ion etching to a depth of 40 nm and subsequent removal of remaining imprint resist by O_2 plasma. To prepare the master wafer for replica molding, it was treated with Repel Silane (Amersham Biosciences) for three hours to facilitate mold separation. An SEM photo and AFM measurement (Figure 2(a-b)) confirm that the master wafer conforms to our design specifications.

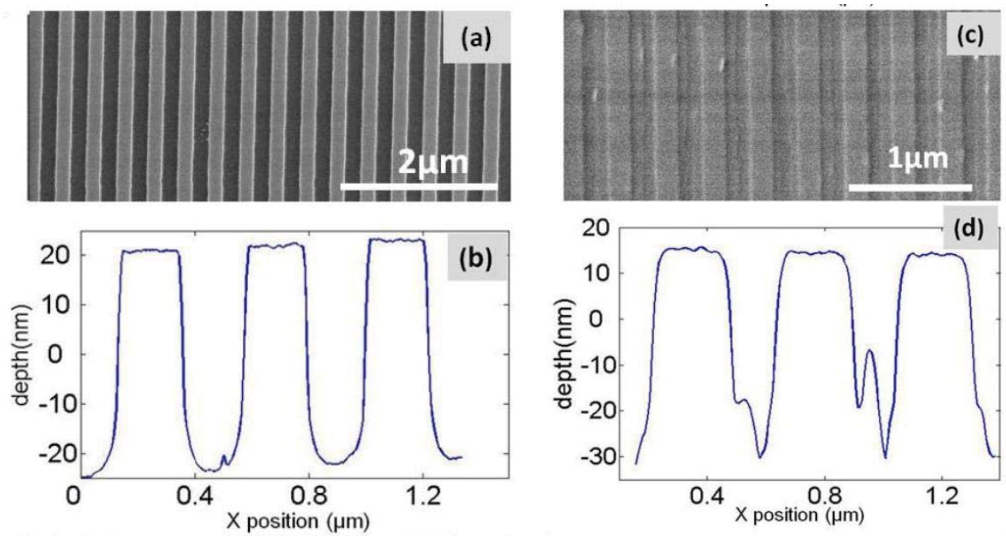

Fig. 2. SEM (a) and AFM (b) images of the master wafer surface, confirming a grating period of Λ=400 nm period, 50% duty cycle on the master wafer. SEM (c) and AFM (d) of the replica molded grating.

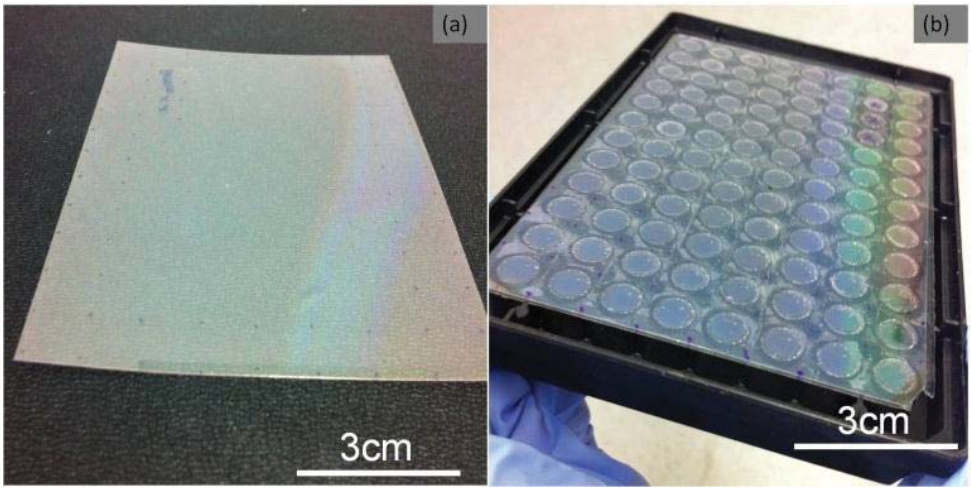

Fig. 3. Photos of DFBLB devices. Before (a) and after (b) the device was bonded to a 96 well bottomless microplate.

Following preparation of the master wafer, a replica molding process is used to transfer a negative volume image of the master wafer to a flexible plastic substrate. The process is performed at room temperature, and requires only low mechanical pressure between the mold and the plastic substrate. A small volume (~1mL) of UV curable polymer (PC409, SSCP Co., Ltd.) selected for its low refractive index (n=1.39, at λ=600 nm after curing) was dispensed onto the surface of the master wafer in a thin line pattern (~150×80 mm2). One edge of a 10×4 cm^2 PET sheet was placed in contact with the polymer, and a ~5 lb. teflon-coated aluminum cylinder was rolled over the PET beginning from the edge of the wafer with the line of polymer. As the cylinder rolled over the PET sheet, the polymer trapped between the sheet and the master wafer was squeezed to a thickness of ~1.5 μm, and the trapped air was expelled towards the leading edge of the advancing liquid front. The liquid polymer conformed to the shape of the master wafer, and was cured to a solid by exposure to a high intensity UV lamp (Xenon) for 50s at room temperature. After curing, the replica was peeled away from the master wafer. SEM and AFM were used to measure the dimensions of the resulting structure (Figure 2(c-d)). Finally, the cured polymer was exposed to O_2 plasma for 3 min to render the surface hydrophobic.

Following replica molding, the horizontal dipping process was used to apply the gain layer. Before the dipping process, the active polymer layer was prepared by mixing a 5 mg/ml solution of Rhodamine 590 dye (Exciton) in CH_2Cl_2 with SU-8 (5.0 wt %; Microchem) to a volume percentage of 10%. This mixture was sonicated for 1min to improve the homogeneity the solution. The viscosity of the solution was measured to be 1.34 cP. The horizontal dipping system consists of a custom-built translatable 1mm-diameter cylindrical barrier and a porous vacuum chuck to hold the PET sheet firmly in place. The porous vacuum chuck (Wenesco Inc.) was made of anodized aluminum and machined flat to 0.005 in. tolerance over its 6x4 $inch^2$ area. With the PET/grating sheet held in place, the dipping solution was injected into the gap (1.2 mm) between the barrier and the PET surface. After 1 min., the solution evenly spread to fill the gap, forming a downstream meniscus via capillary force. Next, the barrier was translated smoothly at a speed of 0.1cm/s using a motorized linear translation stage, leaving a thin film of the dye-doped solution on the grating substrate. After the dipping process, the coated device was soft baked on a 95 °C hotplate for 1 min. to remove the solvent. Finally, the film was photopolymerized by exposing to UV radiation (λ = 365 nm lamp source) with exposure dose of 100 mJ cm^{-2}, and subsequently hard baked on a 95 °C hot plate for 2 min. Figure 3(a) shows the device after the horizontal dipping process. The process slightly planarized the grating surface, resulting in periodic surface features of only 1 nm height as measured by AFM (data not shown).

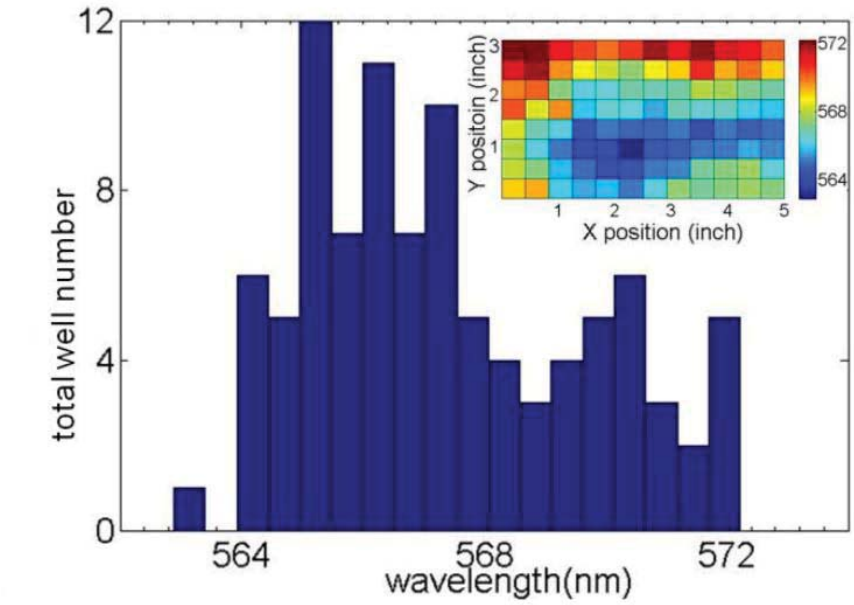

Fig. 4. Histogram of laser emission wavelengths from center region of 96 wells over the DFBLB microplate. The calculated standard deviation was σ=2.35 nm while the mean lasing wavelength was λ_{mean}=568.50 nm, corresponding to a coefficient of variation of CV=0.41%. Inset shows spatial distribution over the device. The color bar represents the emission wavelengths, which varied by as much as Δλ≈9 nm over the whole area, corresponding to ~40 nm thickness variance.

The final fabrication step is deposition of a 10 nm thick layer of TiO_2 over the horizontal-dipped layer using an electron beam evaporator (Denton Vacuum) to improve biomolecular immobilization and sensor sensitivity as demonstrated in previous research [18, 19]. The finished device was trimmed to a 3x5 inch^2 "coupon" that was attached with a die-cut pressure-sensitive adhesive sheet to a bottomless 96 well microplate. In the finished device (Figure 3(b)), the 6 mm diameter bottom surface of each microplate well is comprised of a DFBLB biosensor.

Detection instrumentation using pulsed laser excitation and spectrometer-based measurement of device laser emission

The detection instrument used in this work has been described in a previous publication [21]. Briefly, the device was optically pumped by a frequency-doubled, Q-switched Nd:YAG pulsed laser (λ=532 nm, 10 ns pulse duration, and maximum repetition rate of 10Hz). The pump source passed through a beam expander and a spatial filter to clean the beam, which was subsequently focused onto a ~4 mm diameter spot on the DFBLB surface by a 10x objective lens. There is no requirement for the device to be illuminated at any specific incident angle, therefore coupling excitation light to the sensor is extremely robust.

The lasing emission was collected by the same 10x objective lens. The collected light passes through a dichroic mirror and a long pass emission filter to eliminate photons at the same wavelength as the pump source. The emission was coupled into a 200 μm diameter optical fiber by a NA=0.25 convex lens to reduce the coupling loss due to the weak confinement in the axis parallel to the grating. The distal end of the fiber was connected to a spectrometer (Horiba, MODEL #550) with a 0.0125 nm resolution between adjacent wavelength data points in the 580 - 600 nm spectral range of the DFBLB. The spectral output of the laser was fitted to a Lorentzian to determine the peak wavelength value (PWV) of the emission with greater resolution than available from the discrete points available from the spectrometer [19].

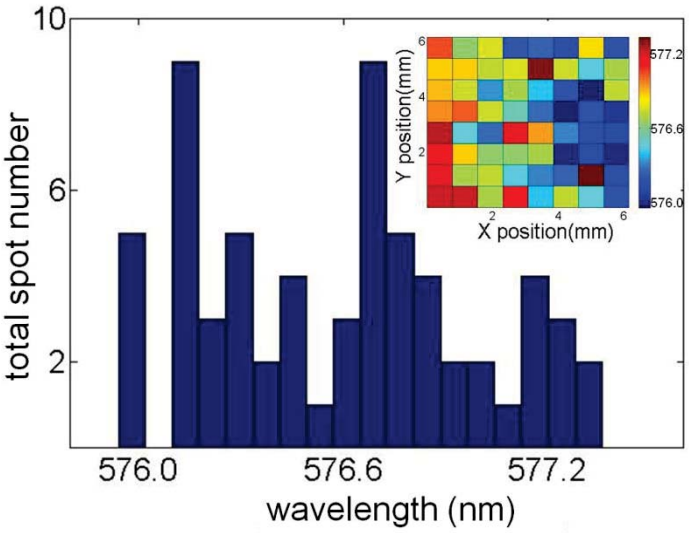

Fig. 5. Histogram of laser emission from 64 points over the 32 mm2 area within one well of a DFBLB microplate. Inset shows spatial distribution. The emission wavelengths varied by as much as $\Delta\lambda \approx 1.38$ nm and the calculated standard deviation was $\sigma = 0.40$ nm with the mean value $\lambda_{mean} = 576.60$ nm, corresponding to a CV=0.07% and a thickness variation of the guidance layer of only ~6 nm.

Results

Film thickness uniformity measured by laser emission wavelength

Due to the relationship between the lasing wavelength and the guidance layer thickness, the uniformity of the device was investigated by the distribution of the emission wavelength. Figure 4 shows the spatial distribution and histogram of the emission wavelength over the microplate area (5×3 inch^2). Measurements were taken at the center of each well and 96 points in total were recorded. The emission wavelengths varied by as much as $\Delta\lambda \approx 9$ nm over the whole area, corresponding to ~40 nm thickness variance as determined via Rigorous Coupled Wave Analysis (RCWA) computer simulations of the device structure. As shown in Figure 4, the overall uniformity can be further improved through the use of a larger substrate, since the variation in the thickness near the edges of the sensor coupon is the primary contributor to the total variance. The calculated standard deviation of lasing wavelength was $\sigma = 2.35$ nm while the mean lasing wavelength was $\lambda_{mean} = 568.50$ nm, corresponding to a coefficient of variation of CV=0.41%. To characterize the uniformity at a finer spatial scale, 64 points within a single well were also measured. Figure 5 shows the distribution of the lasing wavelength over the ~32 mm^2 area within one well. The emission wavelengths varied by as much as $\Delta\lambda \approx 1.38$ nm and the calculated standard deviation was $\sigma = 0.40$ nm with the mean value $\lambda_{mean} = 576.60$ nm, corresponding to a CV=0.07%. This corresponds to a thickness variation of the guidance layer of only ~6 nm.

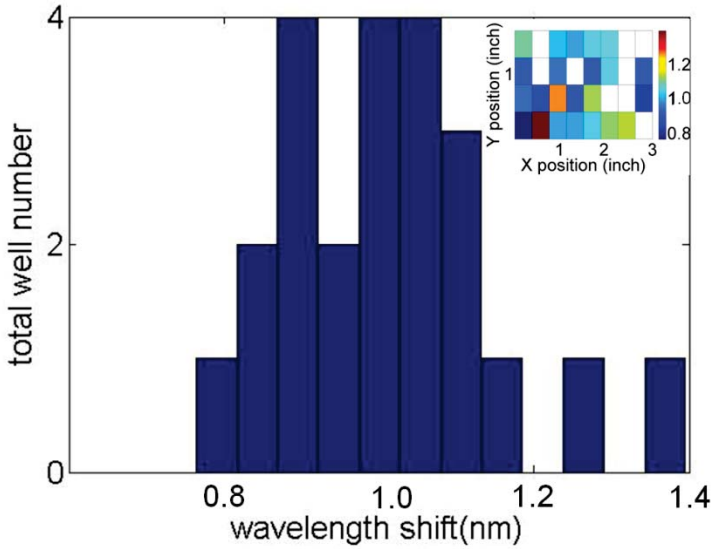

Fig. 6. Histogram of laser wavelength shifts from center of 32 wells due to adsorption of a PPL monolayer. Wavelength shift of 1.01±0.13 nm with CV≈13.60% for the polymeric monolayer was observed. Inset shows the spatial distribution of the wavelength shift for the 32 wells. The blank squares represent locations where the emitted bandwidth had broadened, due to the inhomogeneous binding of the protein polymer Poly (PPL).

Sensitivity uniformity measured by response to adsorption of a protein monolayer

The sensor's bulk sensitivity and uniformity of surface sensitivity were studied by applying liquids with different refractive indices to the sensor surface and measuring the resulting laser PWV shift. To study the device's "bulk" sensitivity, the sensitivity to changes in the refractive index (RI) of media exposed to the sensor surface was measured by placing ~100µL of water (RI=1.33), 35% glycerol (RI=1.37), 55% glycerol (RI=1.41) and 75% glycerol (RI=1.44) in 4 different wells. The recorded laser wavelengths were plotted as function of liquid RI in (data not shown) and a bulk RI sensitivity of $Sb = \Delta\lambda/\Delta n$ was calculated for each well, where Δn is the index change of the medium and $\Delta\lambda$ is the wavelength shift. The average bulk sensitivity over 4 wells was 92.75 nm/RIU, where RIU is the refractive index unit, and the standard deviation was as small as 0.22 nm/RIU. While the bulk sensitivity measurement is a common metric for optical sensors, probing the device response to surface-based binding is a more useful method to study the performance of the biosensor in the context of a biomolecule binding application. To characterize the near-surface sensitivity, lasing wavelength shifts due to the absorption of a monolayer of protein polymer Poly (Lys, Phe) (PPL, 1mg/mL; Sigma-Aldrich) were measured for 32 wells. Measurements were taken in the center of each well and results are summarized and compared in Figure 6. We observed a PWV shift of 1.01±0.13nm with CV≈13.60% for the polymeric monolayer. Additionally, in order to characterize the device's short-range uniformity of sensitivity to surface mass absorption, 64 points within one well were also measured and these results are shown in Figure 7. The calculated standard deviation was σ=0.10 nm, the mean value was λ_{mean}=0.84 nm, and the corresponding CV was 11.79%. Detection instrument used in this work has been described in a previous publication [21]. Briefly, the device was optically pumped by a frequency-doubled, Q-switched Nd:YAG pulsed laser (λ=532 nm, 10 ns pulse duration, and maximum repetition rate of

10Hz). The pump source passed through a beam expander and a spatial filter to clean the beam, which was subsequently focused onto a ~4 mm diameter spot on the DFBLB surface by a 10x objective lens. There is no requirement for the device to be illuminated at any specific incident angle, therefore coupling excitation light to the sensor is extremely robust.

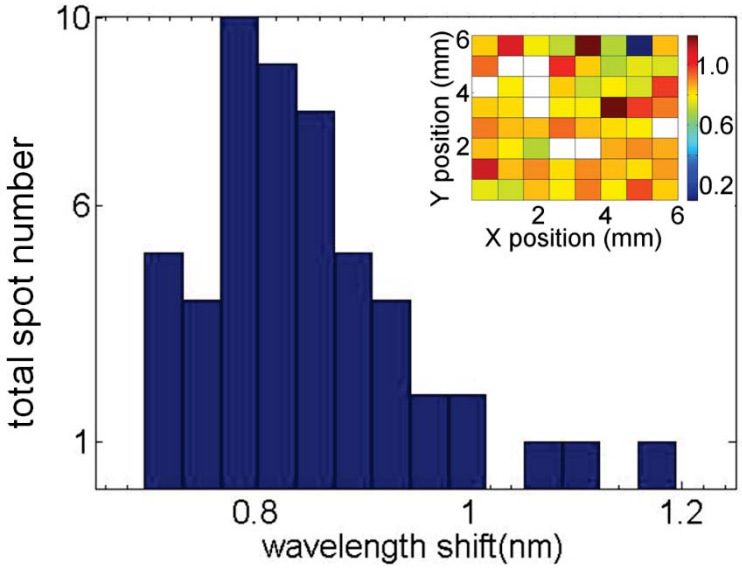

Fig. 7. Histogram of laser wavelength shifts from 64 points within one well due to deposition of a PPL monolayer. The calculated standard deviation was σ=0.10 nm, the mean value was λmean=0.84 nm, and the corresponding CV was 11.79%. Inset shows the spatial distribution of the PPL shift.

Application to an assay for detection of TNF-α

To demonstrate the ability of the sensor to detect biomolecules in the context of a binding assay, four different wells in the sensor microplate were first rinsed and soaked in Phosphate buffered saline (PBS) buffer to establish an initial baseline emission wavelength. To functionalize the sensor surface, each well was treated with a 10% solution of polyvinylamine (PVA; provided by SRU Biosystems Inc.) in water and incubated at 40 ºC for 2 hours. All wells were then washed 3 times with water. Each well of the sensor was then exposed to 50 µL glutaraldehyde solution (25% in water; Sigma–Aldrich) for 4 hours, followed by a wash step. Next, a measurement of the emission wavelength from the PBS-immersed laser surface was made and recorded. A 40µL volume of anti-TNF-α (Biolegend; MW=55 kDa) was then pipetted into four wells separately, and allowed to incubate for 30 min at 4C. After rinsing 3x with a solution of PBS with 2% tween (PBST) to remove unbound anti-TNF-α, the emission wavelength from the center spot of each well was measured and wavelength shifts compared to the end point of the previous step were calculated. 40µL of protein-free blocker (Bio-Rad Laboratories) was applied into each well subsequently and allowed to stabilize for 2 hours at room temperature. The spectrum was recorded again as the reference after the surface was washed by PBST. TNF-α (R&D Biosystems Inc.; MW=17 kDa) was dissolved in a 50mL solution of PBS to four different concentrations (5, 2.5, 1.25 and 0.625 µg/mL), and applied separately to each well and stabilized for 30 min. Next, the sensor surface was rinsed with PBST solution to remove any unbound TNF-α. Figure 8 shows the laser wavelength shift end point as a function of TNF-α concentration. The highest concentration (5µg/mL) of TNF-α detection approaches saturation due to the limited number of anti-TNF-α sites on the sensor surface. The lowest concentration of TNF-α (0.625µg/mL)

resulted in the measured laser wavelength shift of ~0.02 nm. As indicated by the inflection point, the dissociation constant Kd was measured to be 1.185µg/mL (0.069 µM), which is comparable with previously measured values of 0.136 µM for human TNF-α and anti-human TNF-α pairs obtained by dual color fluorescence cross correlation spectroscopy [25].

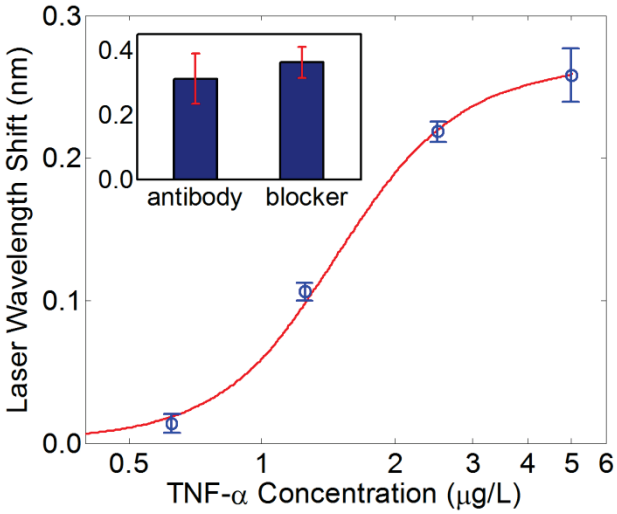

Fig. 8. Laser wavelength shift end point as a function of TNF-α concentration. Inset shows wavelength shift due to surface absorption of anti-TNF-α and protein-free blocker.

IV. KEY RESEARCH ACCOMPLISHMENTS

- Production of DFB biosensor surfaces has been demonstrated uniformly over surface areas substantial enough to incorporate into standard format microplates.
- Incorporation of a label-free sensor into a microplate format represents an important step in the development of a technology that can be accepted into pharmaceutical high throughput screening, as this liquid handling method is heavily utilized for assay automation and integration with standard liquid handling systems.

V. REPORTABLE OUTCOMES (papers in preparation)

- Plastic-based distributed feedback laser biosensors in microplate format," Y. Tan, A. Chou, C. Ge, M. Lu, W. Goldshlag, J. Huang, A. Pokhriyal, S. George, and B.T. Cunningham, IEEE Sensors Journal, Accepted, July 2011.

- C. Ge, J. Zheng, C.Wagner, M. Lu, B. T. Cunningham and J. G. Eden, "Optically tunable ring external-cavity laser", IEEE photonics conference, Arlington VA, October 2010.

- Tan, Y.; Ge, C.; Chu, A.; Lu, M.; Goldshlag, W.; Huang, C.; Pokhriyal, A.; George, S.; Cunningham, B.; "Plastic-Based Distributed Feedback Laser Biosensors in Microplate Format," Sensors Journal, IEEE, vol.PP, no.99, pp.1, 0 doi: 10.1109/JSEN.2011.2163933

VI. CONCLUSION

The fabrication process described in this work demonstrates, for the first time, the ability to produce DFB biosensor surfaces uniformly over surface areas substantial enough to incorporate into standard format microplates. Although the fabrication was carried out in a laboratory setting, all methods are compatible with extension of the process to a roll-based manufacturing paradigm. In particular, the nanoreplica molding approach used in this work has been implemented upon continuous rolls of plastic film in a step-repeat process that can utilize a master wafer for thousands of iterations without damage [4, 5], while accurately patterning features in the size scale of 40-150 nm. Likewise, the horizontal dipping process used to generate the dye-doped SU8 layer of the DFBLB has been implemented without the need for spin-coating, while still maintaining excellent control of the layer thickness and uniformity. Incorporation of a label-free sensor into a microplate format represents an important step in the development of a technology that can be accepted into pharmaceutical high throughput screening, as this liquid handling method is heavily utilized for assay automation and integration with standard liquid handling systems. Because the DFBLB grating is semi-continuous, the same sensor format can also be integrated into higher throughput 384-well and 1536-well microplates, which share the same device area as the 96-well microplate demonstrated here. Of course, the DFBLB is not limited to use in a microplate format, as it can also be incorporated into the surface of microscope slides, flasks, tubing, test tubes, or microfluidic channels. A substantial advantage of the DFBLB sensor surface is that any region on the surface is a sensor, and as a result, capture molecules and illumination can occur at any location. The pump source is not required to enter the device at any particular illumination angle, and only has the requirement of containing a wavelength that overlaps the excitation spectrum of the DFB laser dye. Therefore, precise coupling conditions are not required, leading to a robust detection platform that is amenable to high throughput measurements. A single 10 ns excitation pulse is sufficient for gathering a measurement, resulting in a rapid detection rate that can be used to gather kinetic information on biomolecular interactions. We also envision a label-free surface scanning detection approach, in which the excitation spot is rastered across the DFBLB surface to generate a spatial map of biomolecular or cellular binding for applications such as label-free microarrays and label-free cell attachment imaging. Our calculations estimate that the liquid volume probed by a single laser pulse can be as small as $\sim 8 \times 10^{-5}$ pL, assuming that the pumping spot size is near the diffraction limit. All these capabilities are predicated upon the ability to produce DFBLB surfaces that are uniform in terms of the lasing wavelength and the device sensitivity.

VII. REFERENCES

[1] G S. Herminjard, L. Sirigu, H. P. Herzig et al., "Surface Plasmon Resonance sensor showing enhanced sensitivity for CO2 detection in the mid-infrared range," Opt. Express, vol. 17, no. 1, pp. 293-303, 2009.

[2] J. Homola, S. S. Yee, and G. Gauglitz, "Surface plasmon resonance sensors: review," Sensors and Actuators B: Chemical, vol. 54, no. 1-2, pp. 3-15, 1999.

[3] K. Nakatani, S. Sando, and I. Saito, "Scanning of guanine-guanine mismatches in DNA by synthetic ligands using surface plasmon resonance," Nat. Biotechnol., vol. 19, pp. 51-55, 2001.
[4] B. Cunningham, J. Qiu, P. Li et al., "Enhancing the surface sensitivity of colorimetric resonant optical biosensors," Sensors and Actuators B: Chemical, vol. 87, no. 2, pp. 365-370, 2002.
[5] I. D. Block, M. Pineda, C. J. Choi et al., "High Sensitivity Plastic-Substrate Photonic Crystal Biosensor," Sensors Journal, IEEE, vol. 8, no. 9, pp. 1546-1547, 2008.
[6] C. Y. Chao, and L. J. Guo, "Polymer microring resonators for biochemical sensing applications," IEEE J. Selected Topics Quantum Electron., vol. 12, pp. 134-142, 2006.
[7] M. S. Luchansky, and R. C. Bailey, "Silicon Photonic Microring Resonators for Quantitative Cytokine Detection and T-Cell Secretion Analysis," Analytical Chemistry, vol. 82, no. 5, pp. 1975-1981, 2010.
[8] A. J. Qavi, and R. C. Bailey, "Multiplexed Detection and Label-Free Quantitation of MicroRNAs Using Arrays of Silicon Photonic Microring Resonators," Angewandte Chemie International Edition, vol. 49, no. 27, pp. 4608-4611, 2010.
[9] I. M. White, H. Oveys, X. Fan et al., "Integrated multiplexed biosensors based on liquid core optical ring resonators and anti-resonant reflecting optical waveguide," Appl. Phys. Lett., vol. 89, pp. 191106, 2006.
[10] I. M. White, H. Oveys, and X. Fan, "Liquid-core optical ring-resonator sensors," Opt. Lett., vol. 31, no. 9, pp. 1319-1321, 2006.
[11] S. Arnold, "Microspheres, photonic atoms, and the physics of nothing," Am. Sci., vol. 89, pp. 414-421, 2001.
[12] S. Arnold, M. Khoshsima, I. Teraoka et al., "Shift of whispering gallery modes in microspheres by protein adsorption," Opt. Lett., vol. 28, pp. 272-274, 2003.
[13] H. C. Ren, F. Vollmer, S. Arnold et al., "High-Q microsphere biosensor analysis for adsorption of rodlike bacteria," Opt. Express, vol. 25, pp. 17410-17423, 2007.
[14] A. M. Armani, R. P. Kulkarni, S. E. Fraser et al., "Label-free, single-molecule detection with optical microcavities," Science, vol. 317, pp. 783-787, 2007.
[15] A. M. Armani, A. Srinivasan, and K. J. Vahala, "Soft lithographic fabrication of high Q polymer microcavity arrays," Nano Lett., vol. 7, pp. 1823-1826, 2007.
[16] F. Vollmer, and S. Arnold, "Whispering-gallery-mode biosensing: label-free detection down to single molecules," Nat Meth, vol. 5, no. 7, pp. 591-596, 2008.
[17] J.-H. Zhang, T. D. Y. Chung, and K. R. Oldenburg, "A Simple Statistical Parameter for Use in Evaluation and Validation of High Throughput Screening Assays," Journal of Biomolecular Screening, vol. 4, no. 2, pp. 67-73, April 1, 1999, 1999.
[18] M. Lu, S. S. Choi, U. Irfan et al., "Plastic distributed feedback laser biosensor," Applied Physics Letters, vol. 93, no. 11, pp. 111113, 2008.
[19] M. Lu, S. S. Choi, C. J. Wagner et al., "Label free biosensor incorporating a replica-molded, vertically emitting distributed feedback laser," Applied Physics Letters, vol. 92, no. 26, pp. 261502, 2008.
[20] R. Kazarinov, and C. Henry, "Second-order distributed feedback lasers with mode selection provided by first-order radiation losses," Quantum Electronics, IEEE Journal of, vol. 21, no. 2, pp. 144-150, 1985.

[21]C. Ge, M. Lu, X. Jian et al., "Large-area organic distributed feedback laser fabricated by nanoreplica molding and horizontal dipping," Opt. Express, vol. 18, no. 12, pp. 12980-12991, 2010.
[22]B. Park, and M.-y. Han, "Organic light-emitting devices fabricated using a premetered coating process," Opt. Express, vol. 17, no. 24, pp. 21362-21369, 2009.
[23]S. Y. Chou, C. Keimel, and J. Gu, "Ultrafast and direct imprint of nanostructures in silicon," Nature, vol. 417, no. 6891, pp. 835-837, 2002.
[24]S. Y. Chou, P. R. Krauss, and P. J. Renstrom, "Imprint Lithography with 25-Nanometer Resolution," Science, vol. 272, no. 5258, pp. 85-87, April 5, 1996, 1996.
[25]L. Borras, T. Gunde, J. Tietz et al., "Generic Approach for the Generation of Stable Humanized Single-chain Fv Fragments from Rabbit Monoclonal Antibodies," Journal of Biological Chemistry, vol. 285, no. 12, pp. 9054-9066, March 19, 2010, 2010.

*****